Stress release process along a crustal fault analogous to the plate boundary: a case study of the 2017 M5.2 Akita-Daisen earthquake, NE Japan

Keisuke Yoshida[1], Taka'aki Taira[2], Yoshiaki Matsumoto[1], Tatsuhiko Saito[3], Kentaro Emoto[1], Toru Matsuzawa[1]

[1] Department of Geophysics, Graduate School of Science, Tohoku University, Japan

[2] Berkeley Seismological Laboratory and Department of Earth and Planetary Science, University of California, Berkeley, CA, USA

[3] National Research Institute for Earth Science and Disaster Resilience, Tsukuba, Japan

Corresponding author: Keisuke Yoshida (keisuke.yoshida.d7@tohoku.ac.jp)

Key Points:

- Relocated hypocenters and focal mechanisms indicate that the mainshock, foreshocks, and aftershocks occur on the same intraplate fault.
- The foreshocks, mainshock, aftershocks, and post-seismic slip released stress on different fault segments.
- Foreshock and aftershock seismicity migrate along the fault plane, suggesting aseismic slip occurs before and after the mainshock.

Abstract

Stress accumulation and release in the crust remains poorly understood compared to that at the plate boundaries. Spatiotemporal variations in foreshock and aftershock activities can provide key constraints on time-dependent stress and deformation processes in the crust. The 2017 M5.2 Akita-Daisen intraplate earthquake in NE Japan was preceded by intense foreshock activity and triggered a strong sequence of aftershocks. We examine the spatiotemporal distributions of foreshocks and aftershocks and determine the coseismic slip distribution of the mainshock. Our results indicate that seismicity both before and after the mainshock was concentrated on a planar structure with N-S strike that dips steeply eastward. We observe a migration of foreshocks towards the mainshock rupture area, suggesting that foreshocks were triggered by aseismic phenomena preceding the mainshock. The mainshock rupture propagated toward the north, showing less slip beneath foreshock regions. The stress drop of the mainshock was 1.4 MPa and the radiation efficiency was 0.72. Aftershocks were intensely triggered near the edge of large coseismic slip regions where shear stress increased. The aftershock region expanded along the fault strike, which is attributed to the post-seismic aseismic slip of the mainshock. The postseismic slip possibly triggered repeating earthquakes with M ~3. We find that the foreshocks, mainshock, aftershocks, and post-seismic slip released stress at different segments along the fault, which may reflect differences in frictional properties. Obtained results were similar to those observed for interplate earthquakes, which supports the hypothesis that the deformation processes along plate boundaries and crustal faults are fundamentally the same.

1. Introduction

Earthquakes are natural phenomena which release stress and strain energy accumulated inside the earth (Knopoff, 1958; Savage, 1969). Interplate earthquakes release the stress accumulated by the slip deficit along the plate interface, while intraplate earthquakes, which occur on multiple three-dimensionally-distributed faults, release stress and strain energy accumulated within the plates. Quantification of stress accumulation and release is required for a comprehensive understanding of the deformation processes that take place in the earth.

The accumulation and release of stress at plate boundaries is relatively well understood compared to that in the crust. At plate boundaries, increase in stress can be monitored as part of geodetic analysis by estimating slip deficit (Savage, 1983; Matsu'ura & Sato, 1989). Analyses of recent dense geodetic network data revealed that the slip deficit rate exhibits substantial spatial variations along the plate boundary (e.g., Suwa et al., 2006; Ryder & Bürgmann, 2008: Noda et al., 2018), which probably reflects variation in frictional properties (Lay & Kanamori, 1981). The stress accumulated at plate boundaries is released by both interplate earthquakes and aseismic slip events, and the rupture areas of large interplate earthquakes correlate well with regions of high slip deficit (Hashimoto et al., 2009). Earthquakes cause slip and release stress at same locations repeatedly (Nadeau and Johnson, 1998; Matsuzawa et al., 2002; Yamanaka and Kikuchi, 2004), indicating that the frictional properties along plate boundaries remain the same over long periods of time.

Furthermore, recent geodetic and seismological studies have revealed that not only earthquakes but also abundant aseismic phenomena occur along plate boundaries (e.g., Ide et al., 2007; Beroza & Ide, 2012). These include post-seismic slip (e.g., Wesson, 1987; Heki et al., 1997; Hsu et al., 2006), pre-seismic slip (e.g., McGuire & Jordan, 2000; Uchida et al., 2004), and episodic aseismic slip events (e.g., Linde et al., 1996; Hirose et al., 1999). The diversity in slip styles at plate boundaries is attributed to heterogeneity in stress state, and frictional and rheological properties of the boundary material (Tse & Rice, 1986; Marone et al., 1991; Matu'ura et al., 1992; Shibazaki & Iio, 2003; Perfettini & Avouac, 2004; Liu & Rice, 2005; Ando et al., 2012). Such aseismic phenomena may also play important roles in the accumulation and release of stress in the crust (e.g., Iio et al., 2002; Meneses-Gutierrez & Sagiya, 2016).

The roles of crustal faults in the accumulation and release of stress, however, are poorly understood compared to interplate faults. One difficulty in the assessment of the temporal evolution of stress on a crustal fault comes from the weakness of the geodetic signal produced by any aseismic slip which may occur along a crustal fault. This is due to the deformation rate in the crust, which is substantially lower than at plate boundaries. However, certain time-dependent aspects of seismicity can be used to extract information about aseismic phenomena. For example, the migration patterns of hypocenters have been used for the detection and quantification of aseismic slip propagation (Vidale et al., 2006; Lohman & McGuire, 2007; Kato et al., 2012) and pore pressure diffusion (e.g., Parotidis, 2003; Yukutake et al., 2011; Chen et al., 2012; Shelly et al., 2013a, b).

The distribution of fault structures in the crust adds further complexity to its stress state. Hypocenters of crustal earthquakes are often scattered three-dimensionally in the bulk crust; this distribution is sometimes referred to as a seismicity cloud. Each earthquake within a seismicity cloud can have different fault plane orientations. Intraplate seismicity does not always occur in a

well-defined plane, but some seismicity clouds in the crust merely represent hypocenter estimation errors. In fact, by performing precise hypocenter relocation, previous studies have succeeded in delineating planar structures from seismicity clouds (e.g., Waldhauser & Ellsworth, 2000; Asanuma et al., 2001; Moriya et al., 2003; Yoshida & Hasegawa, 2018a, b). On the other hand, some diversity in hypocenter distribution reflects the true nature of fault structures (e.g., Kilb & Rubin, 2002; Yoshida et al., 2014 and 2015; Ross et al., 2017a, 2019; Xue et al., 2018). In general, larger earthquakes cause larger stress changes further from the fault plane and trigger more off-fault seismicity. This results in a more complex aftershock distribution. We anticipate that this problem can be avoided, and essential information regarding crustal stress accumulation and release can be gathered, by examining a moderate-sized (M~5) earthquake in detail.

In this study, therefore, we examine the spatiotemporal distribution of precisely relocated hypocenters of foreshocks and aftershocks and the coseismic slip distribution of the 2017 M5.2 Akita-Daisen earthquake in NE Japan, to shed light on processes that release stress in the crust. Our results indicate that (1) the foreshocks, mainshock, aftershocks, and post-seismic slip all released stress at different segments of the fault, and (2) much like interplate earthquakes, there are aseismic phenomena behind the occurrence of this M5 intraplate earthquake.

2. The 2017 M5.2 Akita-Daisen earthquake

The 2017 M5.2 Akita-Daisen earthquake occurred on Sep. 8th, 2017 in Akita-Daisen, a northern part of inland NE Japan (Fig. 1), at a depth of about 10 km. This paper refers to the event as the Akita-Daisen earthquake. This earthquake is the largest to have occurred in the northern part of NE Japan since the 2011 M9 Tohoku-Oki earthquake. The focal area is surrounded by the national dense seismic network (Fig. S1 [a]). The moment magnitude and centroid depth listed in the F-net moment tensor catalog (Fukuyama et al., 1997) is Mw 4.9 and 5 km, respectively.

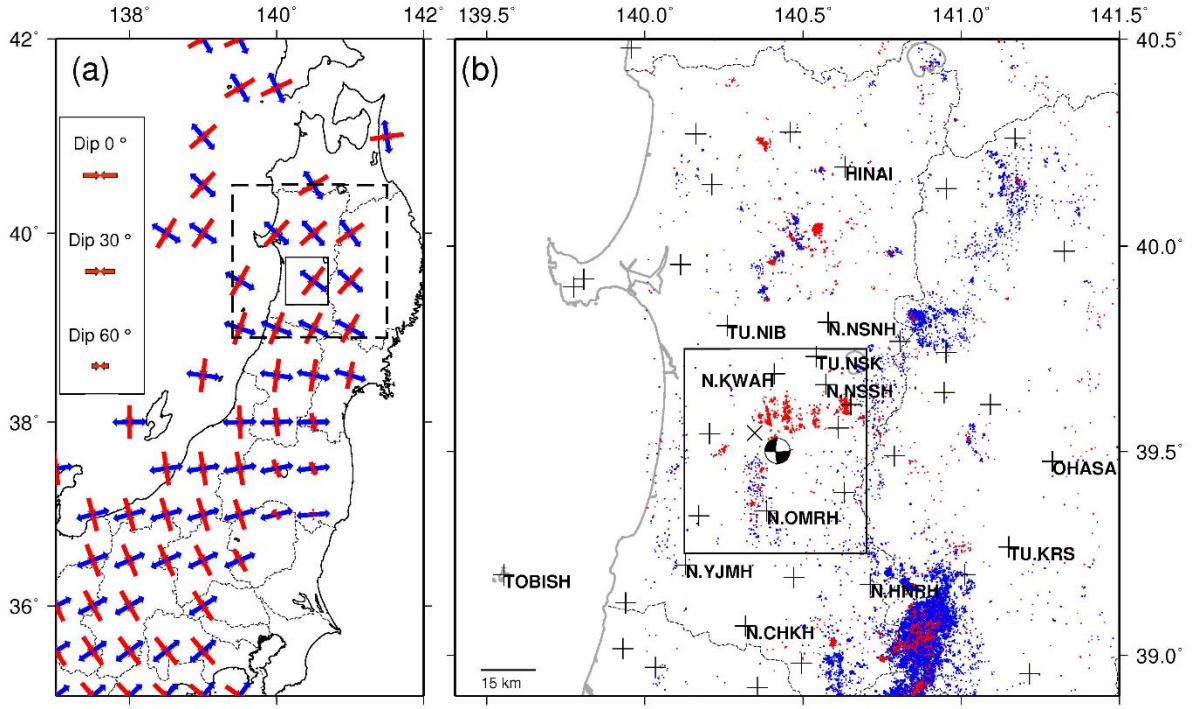

Figure 1. The location of the focal region of the 2017 M5.2 Akita-Daisen earthquake. (a) Orientations of the maximum and minimum principal compressional axes of the static stress change of the 2011 Tohoku-Oki earthquake are indicated by red and blue bars, respectively. The length of the bar corresponds to the plunge of the principal stress axes. The static stress change was computed by Yoshida et al. (2012) using the coseismic slip model of Iinuma et al. (2011). The broken and solid rectangles indicate the range of the map shown in Fig. 1 (b) and Fig. 4 (a), respectively. (b) Hypocenters of earthquakes that occurred before (blue) and after (red) the 2011 Tohoku-Oki earthquake. Plus symbols represent seismic stations. Station names are shown only for stations used for the waveform inversion. The x-mark indicates the location of the nearest KiK-net station (AKTH16). The solid rectangle denotes the area shown in Fig. 2 (a). The 'beach ball' symbol shows the focal mechanism of the mainshock listed in the F-net catalog.

The hypocenters of 554 seismic events with $M_{JMA} \geq 1$ are shown in Fig. S1 (b)–(k). They are listed in the JMA (Japan Meteorological Agency) unified catalog for the period from Jan. 1, 2003 to Dec. 31, 2018. Their depths range from 8 to 12 km. They show a cloud-like spatial distribution across a diameter of a few kilometers, and no planar structure can be observed.

Around the focal region, the stress field was estimated to have rotated > 90° after the 2011 Tohoku-Oki earthquake, transitioning from a dominantly E–W compressional reverse-fault regime to a NNE–SSW compressional strike-slip fault regime, because of the static stress change

(1 MPa of differential stress) caused by the earthquake (Fig. 1 [a]). If this is the case, the differential stress magnitude in the region should be less than 1 MPa (Yoshida et al., 2012). Subsequent studies, however, have suggested the possibility that the observed stress rotation in this region is the product of heterogeneity in stress fields (Yoshida et al., 2019a).

The moment tensor solution of the Akita-Daisen earthquake shows a NE–SW compressional strike-slip earthquake, according to the F-net moment tensor catalog, which is consistent with the stress field produced by the 2011 Tohoku-Oki earthquake (Fig. 1 [a]). Seismicity drastically increased in and around the focal region of the Akita-Daisen earthquake immediately after the 2011 Tohoku-Oki earthquake (Fig. S2). The shear stress magnitude on the fault plane of the Akita-Daisen earthquake increased continuously after the 2011 Tohoku-Oki earthquake occurred (Fig. S3) due to post-seismic deformation, which probably contributed to the occurrence of the Akita-Daisen earthquake.

3. Methods

3.1. Hypocenter relocation

We precisely determined the earthquake hypocenters shown in Fig. S1 (a). We followed the procedure outlined in Yoshida & Hasegawa (2018a). We first extracted the P-wave (49,070 picks) and S-wave (47,566 picks) differential arrival time data from the JMA unified catalog. We also used waveform data obtained at stations close to the source area (Fig. S1 [a]) for the waveform correlation measurements. The stations are three-component velocity seismometers with a sampling rate of 100 Hz, operated by Tohoku University, JMA and Hi-net (Okada et al., 2004). We applied a bandpass filter of between 5 and 12 Hz, and computed the cross-correlation function. Derived differential arrival times were only used if the cross-correlation coefficient was higher than 0.8. The number of differential arrival time data for P- and S-waves, derived from waveform cross-correlation delay measurements, was 175,817 and 204,395, respectively.

We then applied the double-difference earthquake relocation method (Waldhauser & Ellsworth, 2000) to differential arrival time data. We assumed the 1-D velocity model of Hasegawa et al. (1978), which was used routinely at Tohoku University to determine hypocenter locations and focal mechanisms for events in NE Japan. The residual of the differential arrival times decreased from 82 to 20 msec during processing. We evaluated the uncertainty in the relative hypocenter locations by recalculating the relocations 1,000 times, based on bootstrap resampling of differential arrival time data. The 95% confidence regions of the relative hypocenter locations of close events (< 1 km) are 0.0005° in longitude, 0.0003° in latitude, and 224 m in depth on average. This method focuses on estimating relative locations of hypocenters, which is consistent with our goal. For absolute locations, however, the hypocenters determined above might be less reliable than those based on absolute arrival time data. We therefore shifted the centroid of relocated hypocenters to the location of the centroid of hypocenters listed in the JMA catalog while maintaining the relative locations.

3.2. Determination of focal mechanisms

We used the amplitudes of direct P- and S-waves (corrected by those of a reference earthquake whose focal mechanism was known) to calculate the focal mechanisms. We followed the procedure outlined in Yoshida et al. (2019b), which utilizes the amplitude ratios of P-, SH-,

and SV-waves by assuming that the medium in the vicinity of the source is homogeneous and isotropic (Dahm, 1996). We limited the distance between target and reference events to less than 3 km. We used the waveform correlation between the target earthquake and a reference earthquake to reliably obtain the amplitude ratio data.

Sixteen focal mechanisms determined and compiled by Yoshida et al. (2012, 2019a) were adopted as reference focal mechanisms. Amplitude ratio was computed at each seismic station if the cross-correlation coefficient is greater than 0.8. If amplitude ratio data were obtained from more than eight different seismic stations, we estimated the moment tensor components. We computed 2,000 focal mechanisms for each target event based on bootstrap resampling of amplitude ratio data. The difference in focal mechanisms from the best-solution was measured by the 3-D rotation angle (Kagan, 1991). If the 90% confidence region was larger than 30°, we discarded the result. Thus, the moment tensor solutions of 273 $M_{JMA} \geq 1$ events were determined.

3.3. Estimation of rupture process

We used seismic waveform data to estimate the coseismic slip distribution of the mainshock. We first removed the site- and path-effects from the observed waveforms and obtained apparent moment rate functions (AMRFs) of the mainshock using the EGF (empirical green function) method (e.g., Hartzell, 1978). We then inverted the AMRFs for the spatiotemporal distribution of fault slip. The procedure is similar to that of Ross et al. (2017b).

3.3.1. Estimation of apparent moment rate functions of the mainshock

We used the iterative time-domain approach developed by Ligorría and Ammon (1999) after Kikuchi & Kanamori (1982) for the deconvolution of waveforms. We used waveforms from the largest M3.4 foreshock, which occurred close to the mainshock hypocenter (< 350 m according to the relocated hypocenters) as EGF. This earthquake has a similar focal mechanism to the mainshock. We hereafter refer to this earthquake as the "EGF event". Examples of strong waveforms of the mainshock and the EGF event obtained at the nearest KiK-net station are shown in Fig. S4. The transverse components of S-waves were used for waveform deconvolution. The cut-off frequency of the low-pass (Butterworth-type) filter used in the algorithm was set to 3 Hz. If the obtained apparent source time function can explain more than 80% of the observed waveforms in terms of variance reduction, we regarded the deconvolution as successful. Fig. 2 shows the AMRFs recorded at 13 different seismic stations. Since the result at the nearest KiK-net station (Fig. S4 [c]) does not fit this criterion (only 73.3% was reproduced), this result was not used for the waveform inversion. However, we can see that the characteristics of the AMRF are quite similar to the results with similar direction (e.g., TU.NIB).

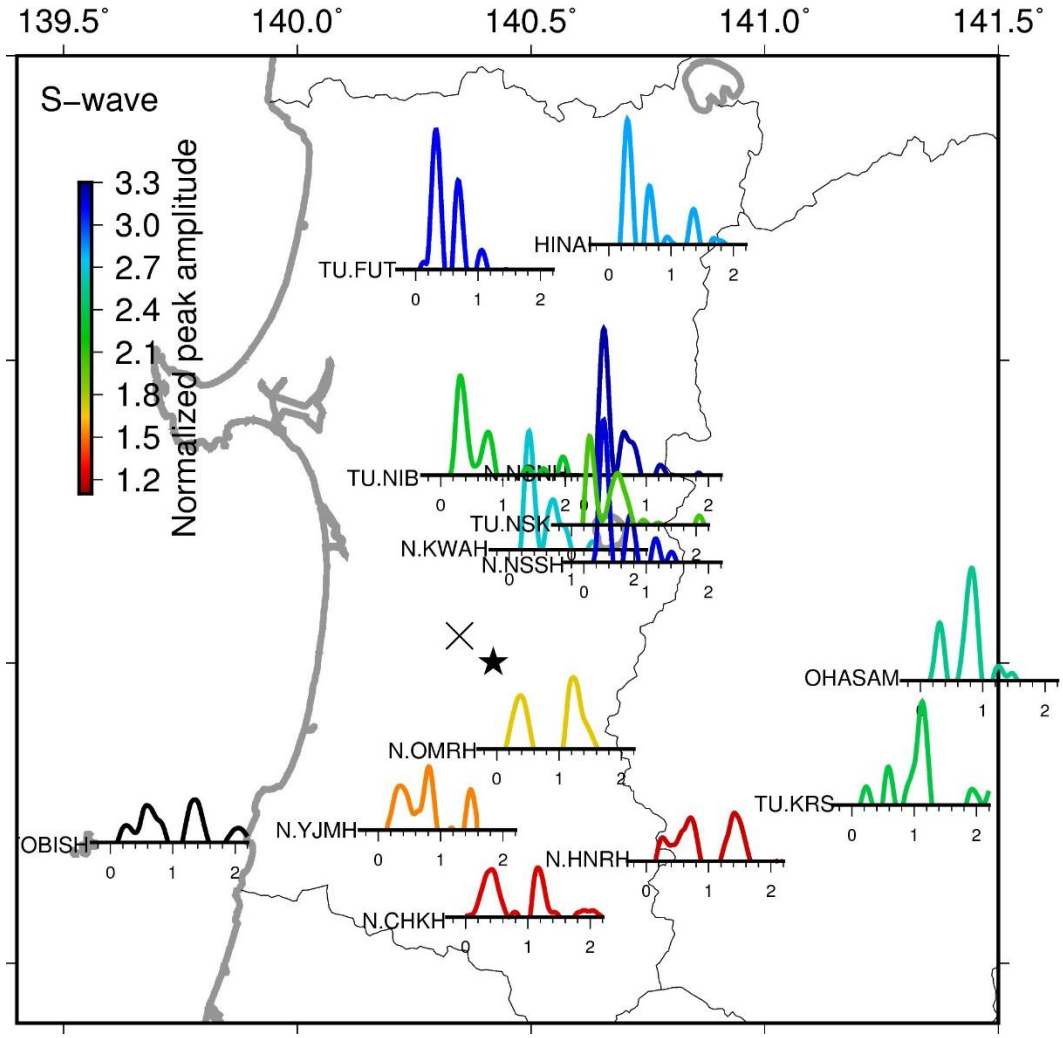

Fig. 2. Distribution of AMRFs computed from waveform deconvolution. The functions are plotted at the locations of the seismic stations and colored according to maximum amplitude. Tick marks denote 0.2 s intervals. The black star denotes the location of the mainshock. Timings of AMRFs are aligned such that the onset of all AMRFs occurs at ~0 s. The x-mark indicates the location of the nearest KiK-net station (AKTH16).

Accurate onset times of AMRFs are necessary to accurately estimate the source process. This requires that the arrival time of the mainshock S-waves is accurately picked; however, this is difficult when the onset is emergent and contaminated by the P-coda wave. In fact, the onset of P-waves implies that slip in the initial stage (~0.1 s) is smaller than slip at the later stage (Fig. S5 [a] and [b]), which suggests that the onset of S-waves also has a small signal. The waveform of the mainshock in the initial stage (−0.1 to 0.1 s in Fig. S5 [b]) is similar to that of the EGF event (Fig. S4 [c]). This supports the result that the distance between the mainshock and the EGF event was small, and may indicate that the mainshock rupture initiated with a similar rupture to that of the EGF event, but finally became larger earthquakes.

We could only pick the onset of the emergent S-wave with confidence using data from a limited number of stations. We assumed that Vp/Vs near the hypocenters of the mainshock and the EGF event were uniform, following Shimamura et al. (2012). We then estimated the differential arrival times of S-waves between the mainshock and the EGF event at each station based on the obtained arrival time of P- and S-waves, and used these estimates as reference points to pick the onsets of S-waves. The relationship between the differential arrival time of P- and S-waves between the mainshock and the EGF event is shown in Fig. 3 (a). The differential arrival times are concentrated on a line which corresponds to uniform Vp/Vs. In Fig. 3 (b), we aligned AMRFs by the mainshock S-wave arrival time thus obtained. The timing of the second pulse can be observed to correlate well with the azimuth.

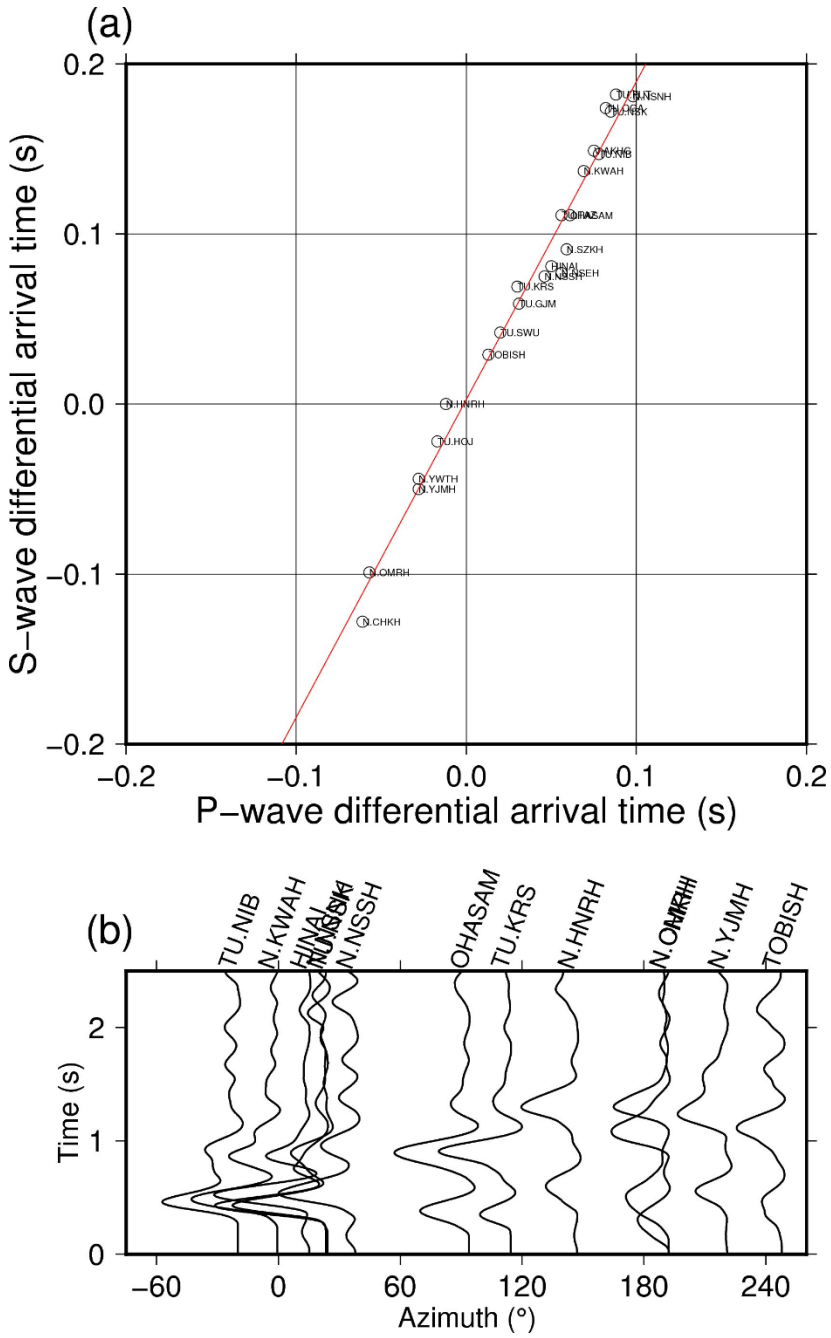

Fig. 3 (a) Differential arrival times of P- and S-waves between the mainshock and the EGF event. The red line indicates the best-fit linear relationship between P- and S-wave differential arrival times. (b) AMRFs aligned by the onset of S-waves.

3.3.2. Finite fault inversion

The AMRFs were inverted to obtain the spatiotemporal distribution of fault slip, following the method of Hartzell & Heaton (1983) and Mori & Hartzell (1990) using the linear equation:

$$d_{obs} = Gm \quad (1)$$

where d_{obs} is the data vector containing the AMRFs, G is the matrix of synthetics, and m is the solution vector of the subfault weights. We assumed that the source nucleated at the single point on the fault surface, and that slip propagated over the fault plane with a constant rupture velocity V_r. We computed the relative delay times between each source node and a given station using the 1-D model formulated by Hasegawa et al. (1978). The fault geometry is assumed to be rectangular with a fault strike of 0° and a dip angle of 80°, based on the mainshock focal mechanism and the hypocenter distribution. We varied V_r/V_s from 0.1 to 0.9, over intervals of 0.1. The length and width of the model fault were set to twice the rupture distance over 2.0 seconds. The model fault was divided into 31 × 31 subfaults. The length and width of each subfault depend on the assumed value of V_r/V_s. For example, they are 396 m in case of V_r/V_s=0.9.

At individual points on the fault, we represented the local moment-rate function as a superposition of five synthetic sub moment rate functions (sMRFs) with different onset timings with regular intervals. The sMRFs were computed by applying the same low-pass filter as that used for the waveform deconvolution to symmetric triangles. The half-duration of the triangles and the time intervals between the onset of the five sMRFs were set to $\mathrm{t_h}$. The initiation timing of the first sMRF was set to when the rupture front reaches the center of the subfault. Their amplitudes were determined in the inversion. We assumed $\mathrm{t_h}$ to be 0.09 s, which corresponds to two thirds of the time necessary for the rupture front to pass one subfault. We introduced a constant damping factor (λ) and a smoothing factor ($\mathrm{e_s}$) with the same value ($\lambda = \mathrm{e_s} = 2$), which was determined based on the trade-off curve (Fig. S6), and employed the nonnegative least-squares algorithm of Lawson and Hanson (1995) to ensure slip positivity.

Fig. S7 (a) shows a comparison of the assumed values of V_r/V_s against the variance reductions VR between the theoretical and observed AMRFs.

$$VR = \sum_{i=1}^{n} \left(1 - \frac{\sum \left(d_{obs}(t_i) - s(t_i)\right)^2}{\sum d_{obs}^2(t_i)}\right) \quad (2)$$

where $d_{obs}(t_i)$ and $s(t_i)$ are the time series of the observed and synthetic apparent moment rate functions, respectively. The best agreement was achieved when V_r/V_s = 0.9, with a variance reduction of 84%. This value falls within the typically-documented range of 0.6–0.9 (Geller, 1976; Lay et al., 2010). The maximum derived slip amount was 14.6 cm.

However, differences in VR are subtle when $\frac{V_r}{V_s} \geq 0.6$, so we cannot reject the values simply based on the fitting of waveforms. Although the assumed value of rupture speed directly affects the spatial extent of the estimated rupture area, the effect is not dramatic in the interval $\frac{V_r}{V_s} \geq 0.6$. Hereafter, we discuss the results of the coseismic slip distribution obtained by assuming V_r/V_s = 0.9. In section 4.2, we show that coseismic slip distribution is not sensitive to changes in the value of V_r/V_s when it is assumed to be ≥ 0.6. Furthermore, since differences in the assumed value of $\mathrm{t_h}$ affect the resultant coseismic slip distribution only slightly, we hereafter assume $\mathrm{t_h} = 0.09$ s.

The measurement error of the initiation timings of P- and S-waves is a possible cause of the estimation error of the coseismic slip distribution. We examined the uncertainty of the coseismic slip distribution using 1,000 simulated AMRF datasets, produced by fluctuating the initiation timings of AMRFs. The probability distribution of fluctuation is assumed to be a uniformly random distribution ranging from -0.15 to 0.15 s. The frequency distribution of VR of 1,000 results based on the simulated datasets is shown in Fig. S8 (a). The mean value and the standard deviation of VR are 76.7% and 4.0%, respectively. The mean value is well below that of the main result (84%), justifying the validity of the initiation timings used for the main result in the scale of added noise. The mean coseismic slip distribution, and the standard deviation of slip amount at each subfault are presented in Fig. S8 (b) and (c), respectively. We also conducted the waveform inversions by shifting the initiation timings of all the AMRFs all together by the same amount from -0.07 to 0.07s. The results are shown in Fig. S9. The results shown in Figs. S8 and S9 are used for the measures of uncertainty of the result.

4. Results

4.1. Fault structure and migration behavior of foreshock and aftershock activities

The distribution of relocated hypocenters is shown in Fig. 4 for the same area as Fig. S1. Most of the relocated hypocenters are distributed on a single planar structure. Figs. 5 and 6 show an enlarged view of the relocated hypocenters and focal mechanisms, respectively.

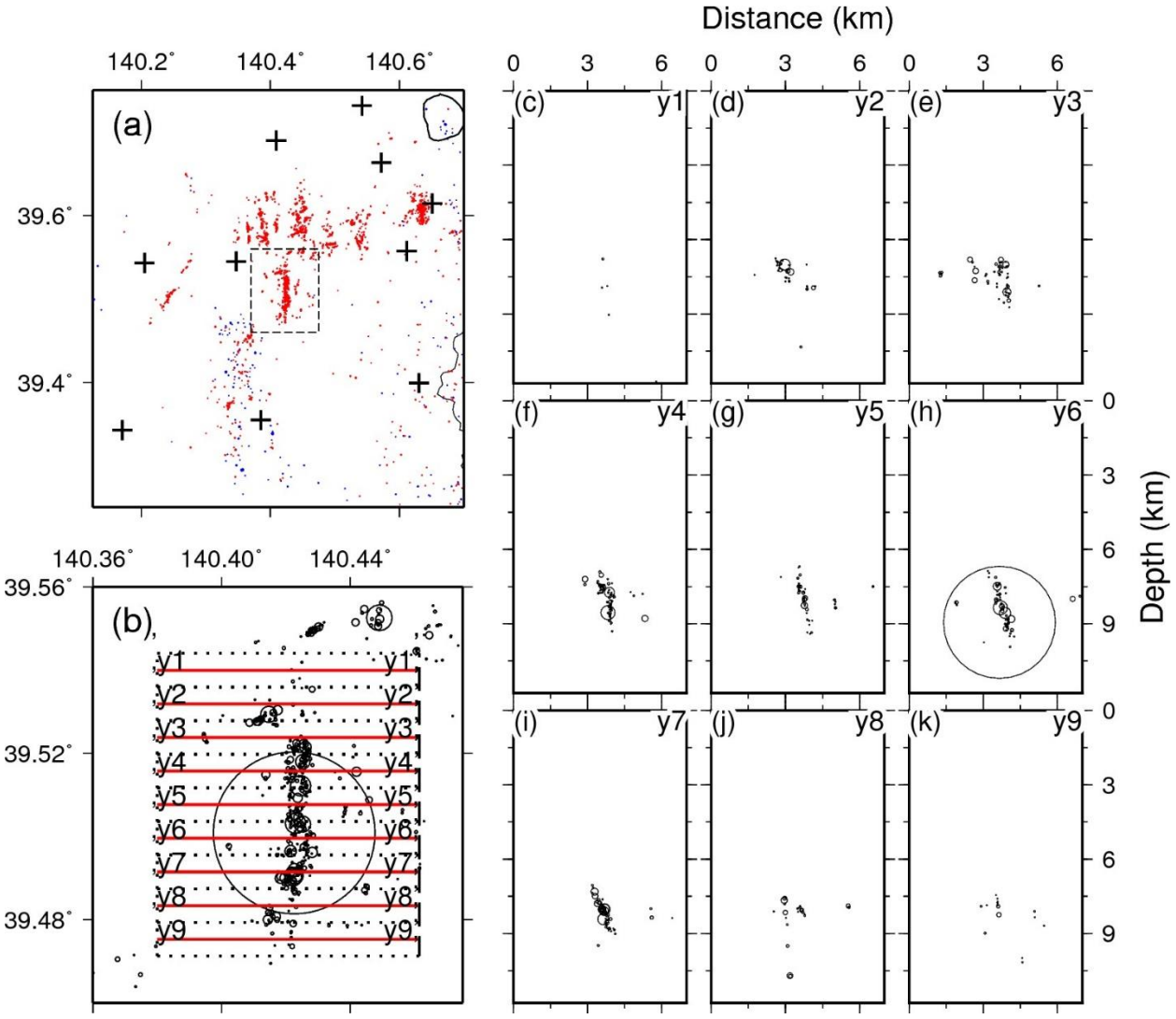

Figure 4. Distribution of the relocated hypocenters. (a) Hypocenters of earthquakes that occurred before (blue) and after (red) the 2011 Tohoku-Oki earthquake. Hypocenters in this region were relocated using the procedure outlined in section 3.1. Plus symbols represent seismic stations. The dashed rectangle denotes the area shown in (b). (b) A map view showing the focal region of the 2017 Akita-Daisen earthquake. (c)–(k) Cross-sectional views of vertical hypocenter distribution along the lines indicated in (b). Black circles represent hypocenters. The size of each circle corresponds to the diameter of the fault, assuming a stress drop of 3 MPa.

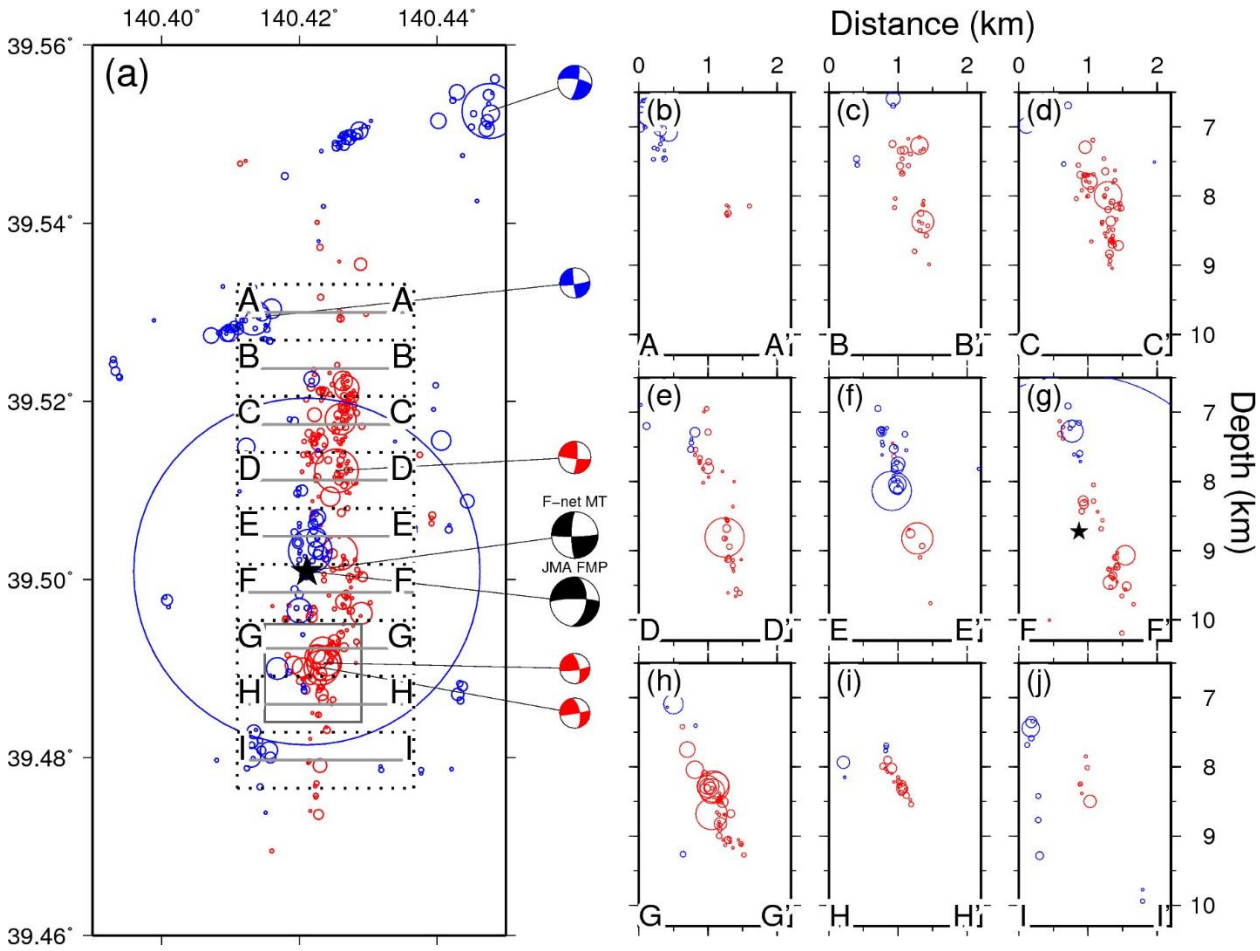

Figure 5. (a) Map and (b)-(j) cross-sectional views (A–I) showing hypocenters (represented by circles) of earthquakes before (blue) and after (red) the mainshock. The size of each circle corresponds to the fault diameter, assuming a stress drop of 3 MPa. Blue and red beach balls show the focal mechanisms derived from the JMA catalog before and after the mainshock. Focal mechanisms were determined from first-motion polarity data. For the mainshock, the first-motion polarity solution listed in the JMA catalog and the moment tensor solution listed in the F-net catalog are shown by black beach balls. The black star denotes the location of the mainshock.

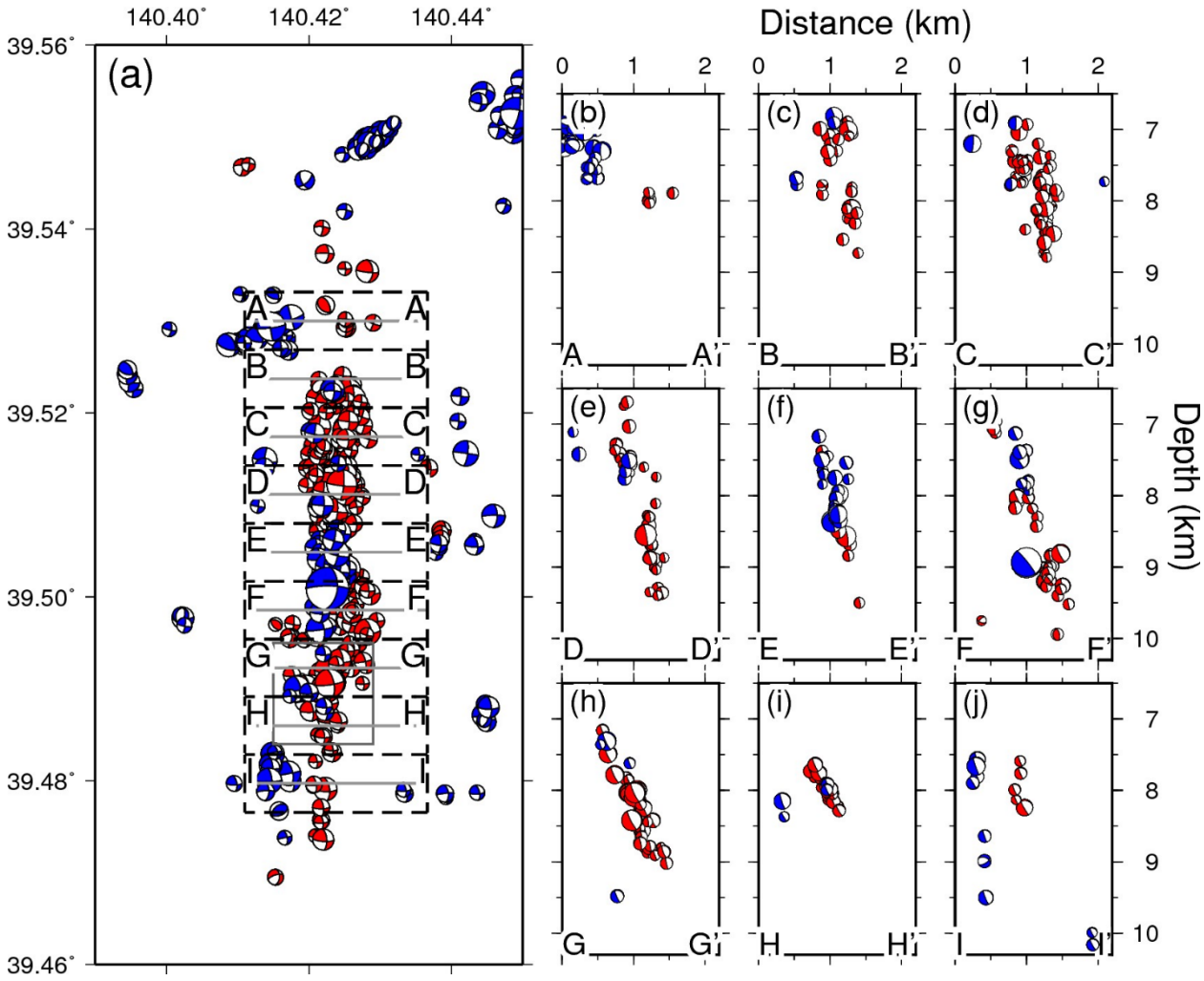

Figure 6. (a) Map and (b)-(j) cross-sectional views (A–I) of focal mechanisms before (blue) and after (red) the mainshock. Beach balls represent focal mechanisms.

The planar distribution of the hypocenters is characterized by N–S strike over a length of 5 km and width of 4 km (Figs. 4 and 5). Its dip is almost vertical in the northernmost cross sections, while it dips towards the east at an angle of ~65–70° to the south. This geometry is consistent with focal mechanisms in this area (Fig. 6), which are characterized by right-lateral strike-slip with almost vertical nodal planes in the north, and nodal planes with similar dip to the hypocenters in the south. These results strongly suggest that individual earthquakes occur on the same macroscopic planar structure.

Two different kinds of focal mechanism are shown for the mainshock in Fig. 5: the first-motion polarity solution listed in the JMA catalog, which represents the fault geometry near the hypocenter, and the moment tensor solution listed in the F-net catalog, which represents the average fault geometry in the entire rupture area. The former has a nodal plane that dips strongly (~65–70°) to the east, which is parallel to hypocenter alignment in the south. The latter has an almost vertical nodal plane and is parallel to hypocenter alignment in the north. This suggests

that the mainshock rupture was initiated in the southern part of the rupture area, and the largest slip occurred in the northern part. Different characteristics of AMRFs between the northern and southern stations (Fig. 2) support this hypothesis. The duration of the first pulse is shorter, the amplitude is higher, and the time interval between the two pulses is shorter (~0.4 s) at the northern stations. The time interval between the two pulses is ~1.2 s at the southern stations. This difference suggests that the first pulse is primarily characterized by northward propagation and the second pulse was produced north of the hypocenter.

Foreshocks and aftershocks appear to have caused slip on different segments of the same plane. Hypocenters of foreshocks, including the largest M3.4 event that occurred on Sep. 9, 2016, are located near the hypocenter of the mainshock (cross-section E in Fig. 5). In contrast, aftershock hypocenters are not distributed near the mainshock hypocenter. Fig. 7 shows a cross-section of hypocenters along the fault strike. A clear seismic gap of aftershocks with a length of about 2 km and a width of about 1 km can be observed around the mainshock hypocenter (Fig. 7 [c]). This seismic gap may represent large slip regions of the mainshock, as reported for larger earthquakes based on the direct comparison of aftershock distribution and coseismic slip distribution (e.g., Mendoza & Hartzell, 1988; Das & Henry, 2003; Woessner et al., 2006; Asano et al., 2011; Ebel & Chambers, 2016; Yoshida et al., 2016; Ross et al., 2017b & 2018; Welzter et al., 2018).

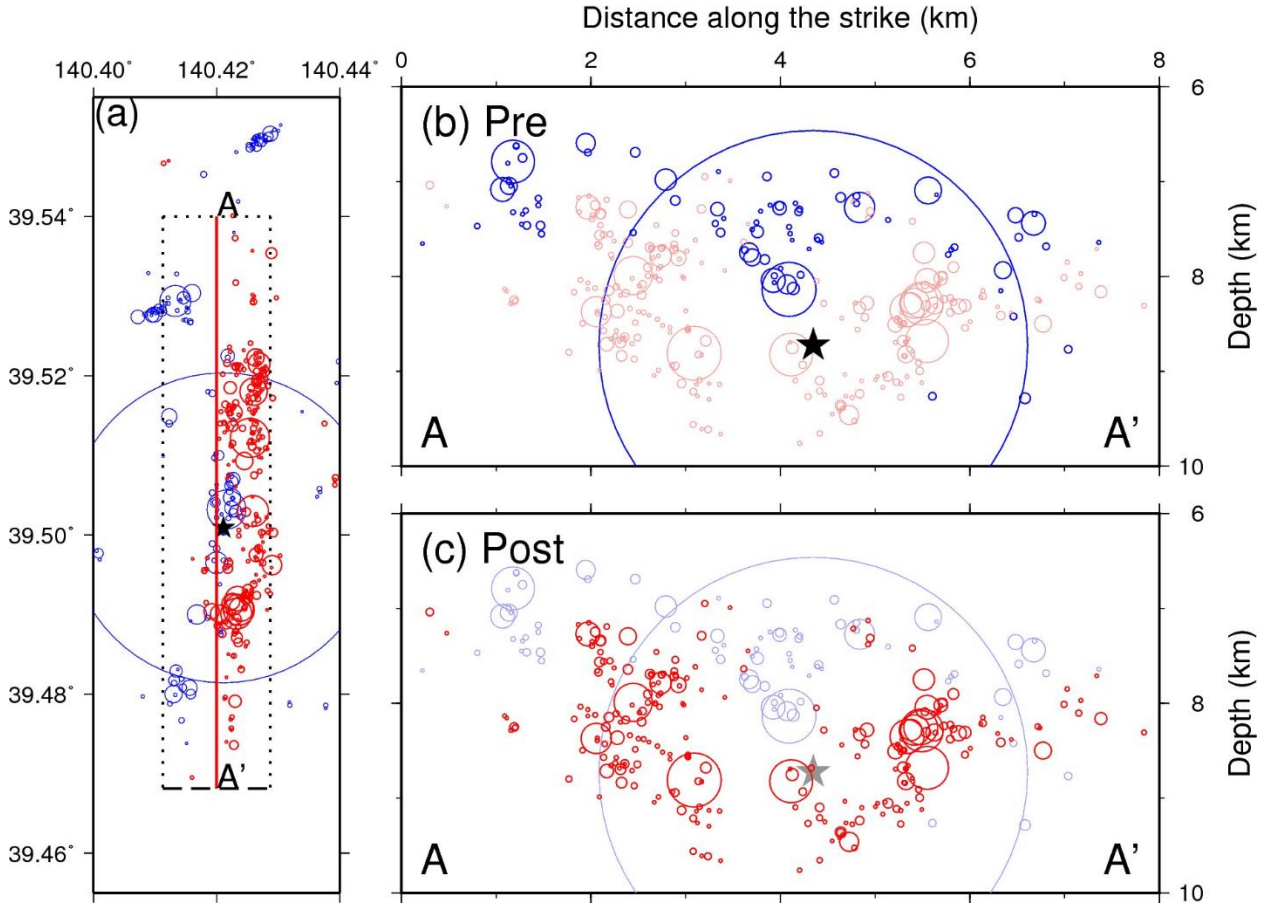

Fig. 7. (a) Map view and (b), (c) cross-sectional views along the strike of the rupture zone showing hypocenters of earthquakes (represented by circles) before (blue) and after (red) the mainshock. The size of each circle corresponds to the fault diameter, assuming a stress drop of 3 MPa. The black star denotes the location of the mainshock.

Fig. 8 shows the time of occurrence of foreshocks with distance along the fault strike from the mainshock hypocenter. The foreshock sequence initiated ~2,000 days before the mainshock, with foreshock hypocenters gradually migrating from north to south. Foreshocks occurred closest to the mainshock hypocenter one year before the mainshock, reaching the area south of the mainshock ~30 days before the mainshock took place (Fig. 8 [b]). Foreshocks migrated back north before the mainshock occurred (Fig. 8 [c]).

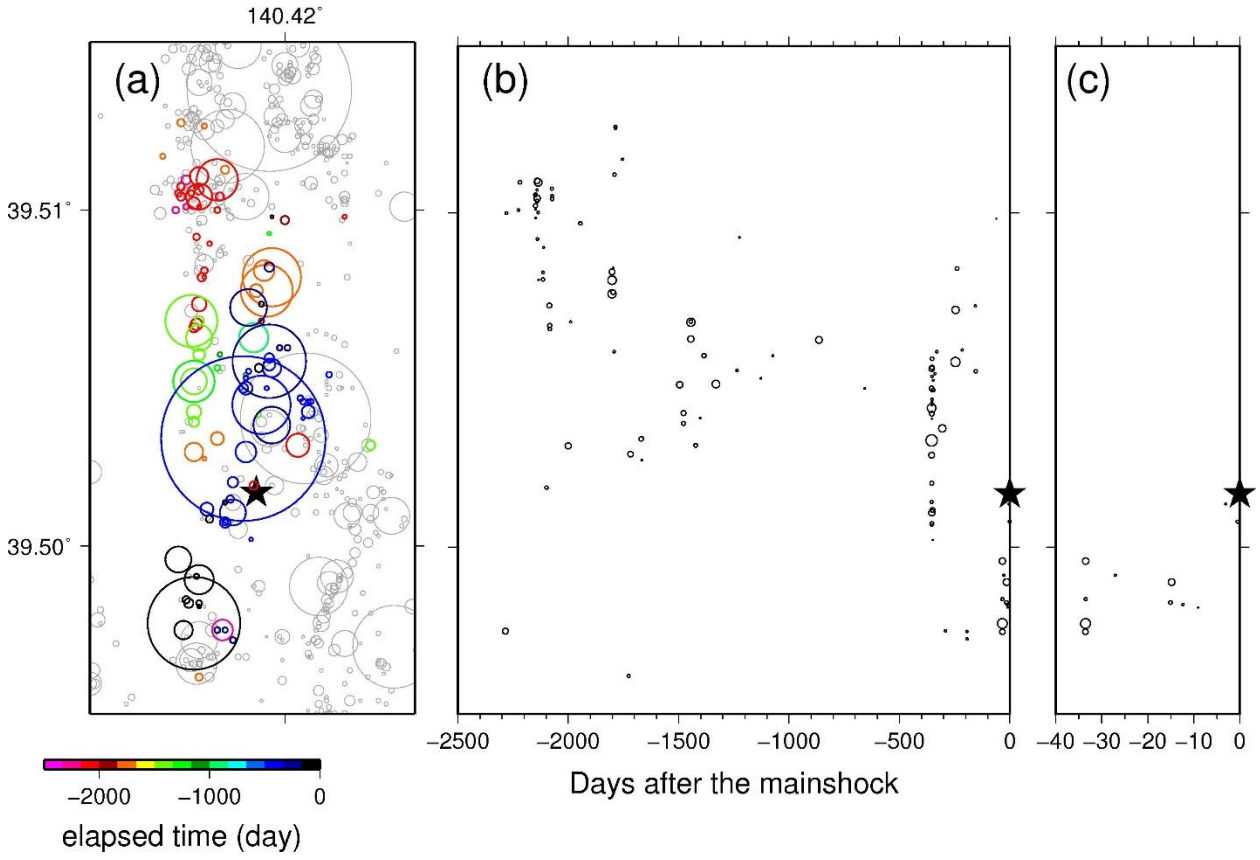

Fig. 8. Temporal variations of hypocenters in the foreshock sequence. (a) Foreshock hypocenters are plotted by time of occurrence according to the color scale. (b)–(c) Time-plots of the latitudes of foreshock hypocenters. Circle size represents earthquake magnitude. The black star indicates the location of the mainshock.

Fig. 9 compares the occurrence timing of aftershocks against the distance along the fault strike. The aftershock area expands with time, especially over the first few days to the southern region. The aftershock region expands approximately with the logarithm of time (Figs. 9 [b] and [c]).

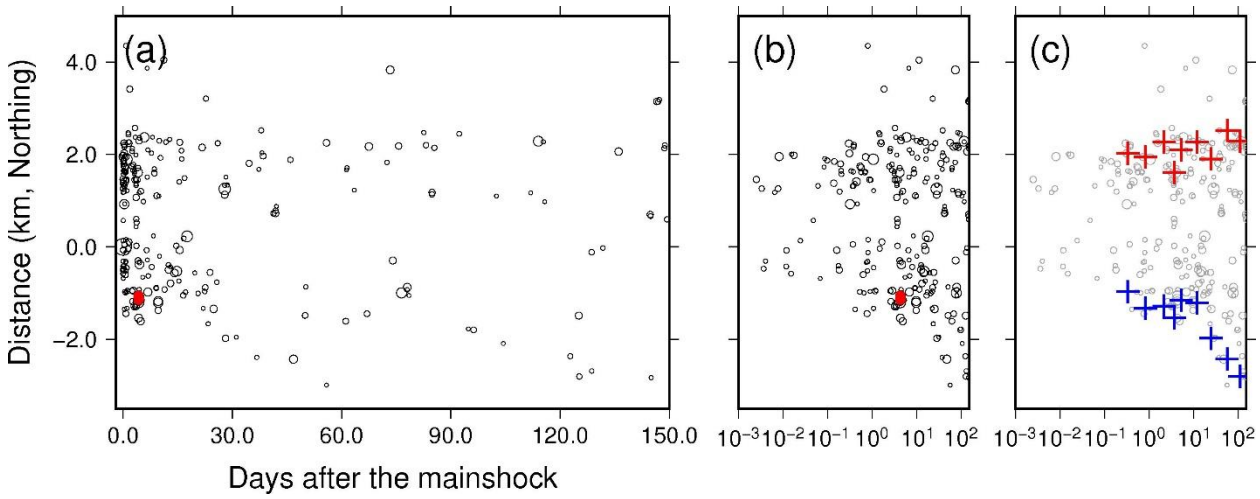

Fig. 9. Time plots of along strike distance of aftershock hypocenters away from the mainshock hypocenter. Circle size indicates earthquake magnitude. Red dots represent possible repeating earthquakes. (a) Distance (km) along the strike as a function of time (days). (b)–(c) Distance (km) along the strike as a function of the logarithm of time (days). In (c), red and blue crosses represent the values at each bin, above and below which 10% of earthquakes occur, respectively. Each bin has the same number of events.

4.2. Coseismic slip distribution of the 2017 M5.2 Akita-Daisen earthquake and its relationship with foreshock and aftershock activity

Fig. 10 shows the final coseismic slip distribution of the mainshock and the moment rate function at each subfault. There are two large slip regions: a region near the hypocenter and a region north of the mainshock hypocenter, which is consistent with what would be expected from the azimuthal dependency of the AMRFs. The distance between the two large slip areas is approximately 1.5 km. Similar characteristics were obtained for the mean result of the 1,000 simulated coseismic slip distributions (Fig. S8 [b]) and the results obtained by systematically shifting the initiation timings of all the AMRFs (Fig. S9); they have two large slip regions near the hypocenter and ~1.5 km north from the hypocenter. Existence of the two slip peaks is significant from the standard deviation of the 1,000 simulated coseismic slip distributions (Fig. S8 [c]). These results indicate that the characteristics of the coseismic slip distribution obtained in this study are robust.

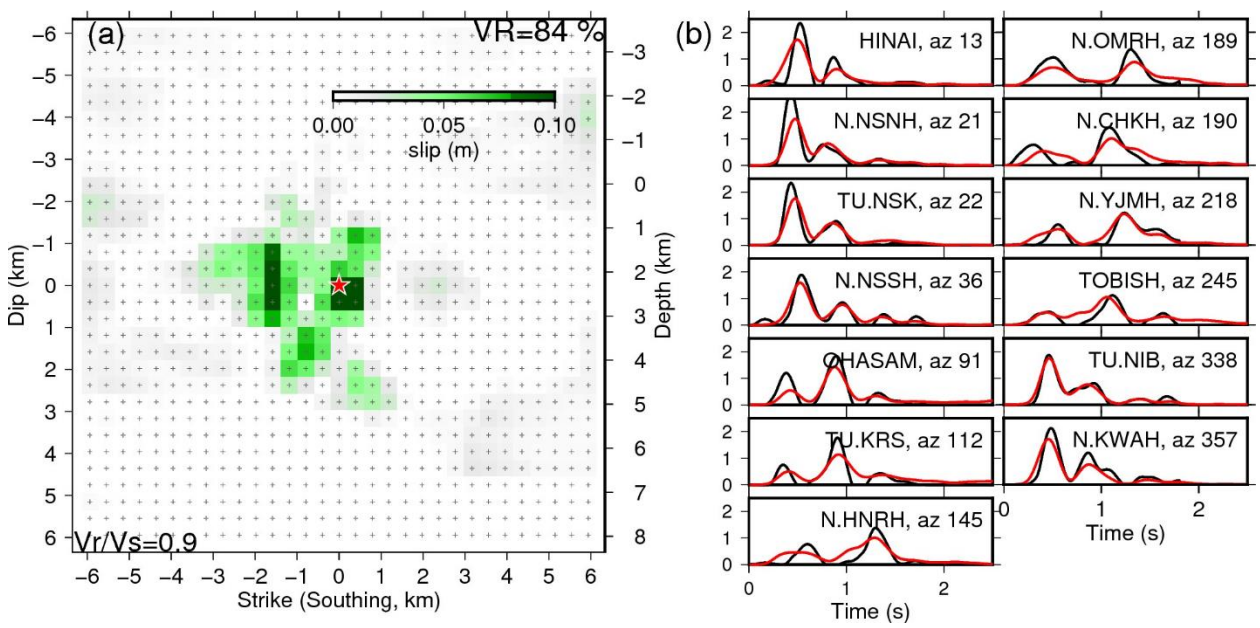

Fig. 10. (a) The coseismic slip distribution obtained assuming Vr/Vs = 0.9. The slip amount is shown by the color scale. (b) Comparison of the observed (black) and synthetic (red) source time functions at each station.

Fig. 11 compares the coseismic slip distribution with the hypocenter distributions. Aftershocks occurred abundantly outside the edges of the two large slip portions (Fig. 11 [b]). The area with a relatively small amount of coseismic slip between two large slip regions corresponds to the deeper extension of intense foreshock activity. Comparisons of the coseismic slip amount against number of foreshocks and aftershocks along the large slip regions are shown in Figs. 11 (c) and (d), respectively. Foreshocks and aftershocks occur at the edges of large slip regions. As a whole, the mainshock, foreshocks, and aftershocks cause slip on different parts of fault. This pattern barely changes if other values of $\frac{V_r}{V_s} \geq 0.6$ are used for the waveform inversion (Fig. S10).

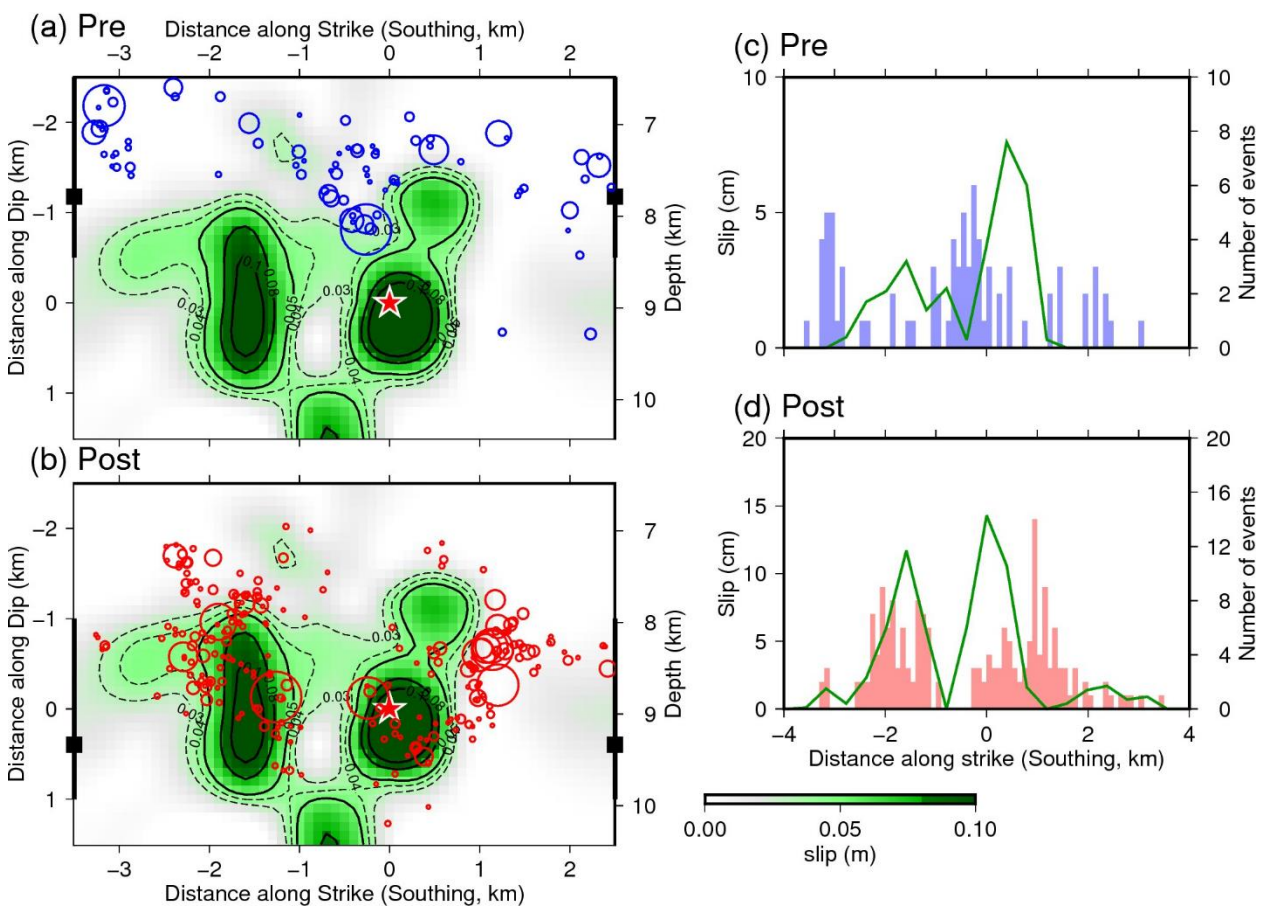

Fig. 11. Comparison of the interpolated coseismic slip distribution (green) against (a) foreshock sequences (blue circles) and (b) aftershock sequences (red circles). Along-strike and along-dip distances are measured with respect to the mainshock hypocenter (black star). In (c) and (d), the amount of coseismic slip (black line) is compared with the number of events before and after the mainshock within the along-strike zone shown by the triangles and bold lines in (a) and (b).

The theoretical equations compiled by Okada (1992) were used to calculate the change in shear stress along the fault, by computing the stress change caused by such a dislocation in a homogeneous elastic half-space. We assumed a Poisson's ratio of 0.25 and a rigidity of 30 GPa. The average stress drop was 1.4 MPa, which was weighted by the slip amount (Shao et al., 2012; Noda et al., 2013). The largest value was 7.0 MPa near the hypocenter. The results are compared with the locations of foreshocks and aftershocks in Figs. 12 (a) and (b), respectively. Aftershocks tend to occur in locations with positive shear stress. The model results showed shear stress change was positive for 75% of M>2 events.

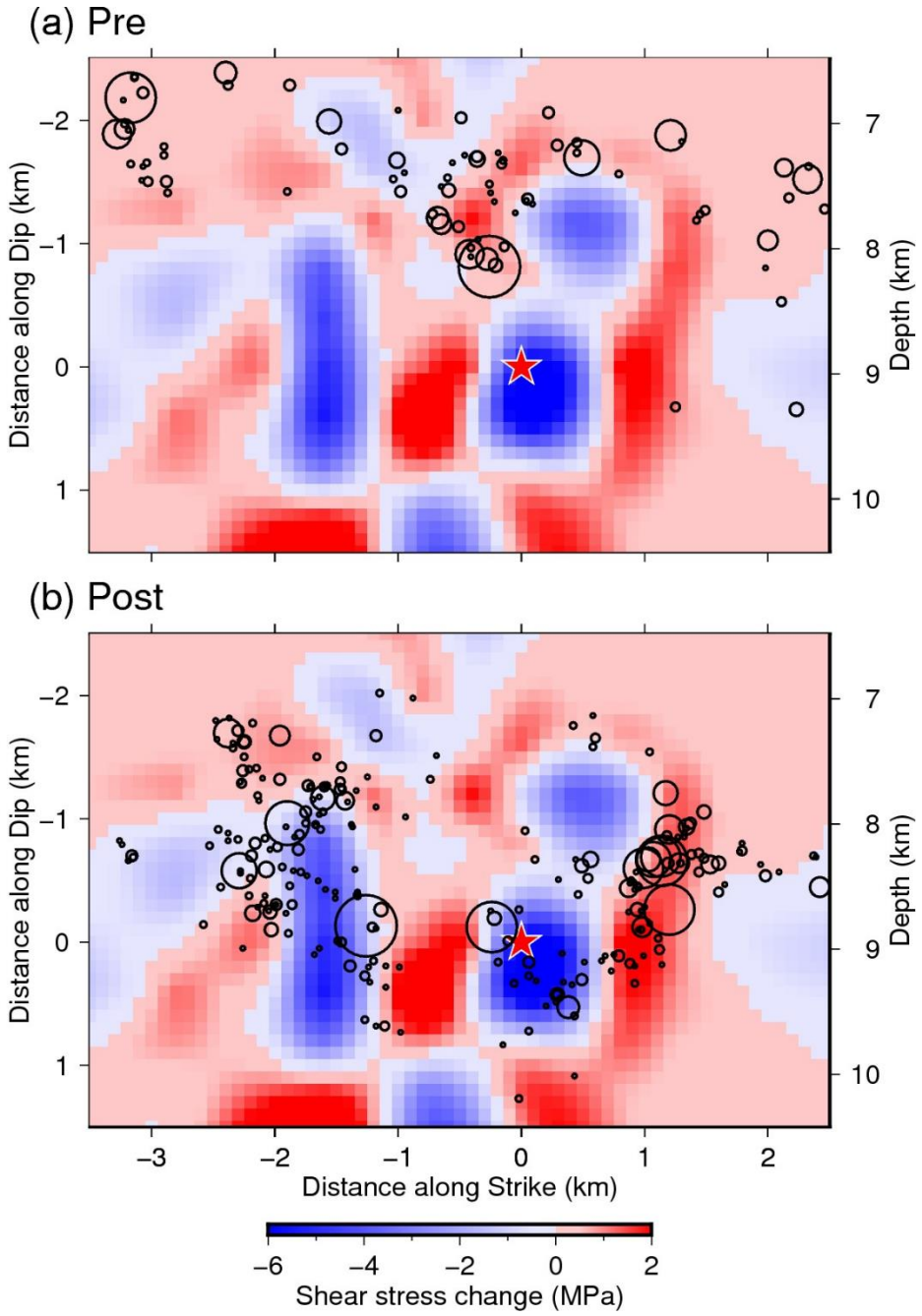

Fig. 12. Comparison of the distribution of shear stress change with (a) foreshock sequences (blue circles) and (b) aftershock sequences (red circles). Along-strike and along-dip distances are measured with respect to the mainshock hypocenter (black star).

We estimated the radiation energy using the method proposed by Vassiliou and Kanamori (1982), which employs the integration of the square of the seismic moment acceleration function. The obtained radiation energy E_R was $4.7 \times 10^{11} J$, which follows that the scaled energy by the seismic moment $\frac{E_R}{M_o}$ was 1.7×10^{-5}. The assumption of a rigidity μ of 30 GPa yielded an apparent stress $\sigma_{ap} = \mu \frac{E_R}{M_o}$ of 0.5 MPa. The radiation efficiency $\eta_R = 2 \frac{\mu}{\Delta\sigma_E} \left(\frac{E_R}{M_o}\right)$ (Kanamori & Rivera, 2006) was approximately 0.72, which falls in the typical range of Mw > 6.7 earthquakes (Venkataraman & Kanamori, 2004). This value is a few times larger than estimates for recent smaller crustal earthquakes such as the 2008 Mw 5.4 Chino Hills, California, earthquake (Shao et al., 2012) and the 2016 Mw 6.2 Tottori earthquake (Ross et al., 2018).

The relatively high radiation efficiency in this study suggests that the Akita-Daisen earthquake occurred on a mature fault. The observation that foreshock and aftershock activities are concentrated on the same planar structure (Fig. 5) supports this idea. The relationship between V_r/V_s and η_R is consistent with that of mode-II cracks (Freund, 1972; Venkataraman & Kanamori, 2004).

5. Interpretation of the results

5.1. Foreshock migration and aseismic process prior to the mainshock

The migration of foreshocks suggests that aseismic processes, such as aseismic slip and fluid migration, proceeded before the occurrence of the mainshock. Aseismic slip has been detected before the occurrence of large interplate earthquakes (e.g., Uchida et al., 2004; Kato et al., 2012; Ito et al., 2013). For example, the migration of foreshocks toward the rupture initiation point of the mainshock was observed in the 2011 Tohoku-Oki earthquake (Ando & Imanishi, 2011; Kato et al., 2012), which was interpreted as the propagation of aseismic slip. It is possible that such aseismic slip also contributes to the occurrence of crustal earthquakes.

Another cause of hypocenter migration is the diffusion of fluid. Earthquake swarm activities triggered by the 2011 M9 Tohoku-Oki earthquake in inland NE Japan were interpreted to be caused by fluid movement facilitated by the earthquake (Terakawa et al., 2013; Okada et al., 2016; Yoshida & Hasegawa, 2018a, b; Yoshida et al., 2018), because their hypocenters exhibited distinct upward migration along planar structures (Yoshida & Hasegawa, 2018a, b), and synchronized temporal variations in seismicity and source parameters (Yoshida et al., 2016c, 2017; Yoshida & Hasegawa, 2018b). Such fluid movement may have preceded the occurrence of the Akita-Daisen earthquake, which in turn may have affected the frictional properties of the source region, causing the earthquake sequence and aseismic slip.

Quasi-static rupture associated with the nucleation of the mainshock is an alternative mechanism for the occurrence and migration of foreshocks (e.g., Dodge et al., 1996; McGuire et al., 2005; Yabe et al., 2015; Yabe & Ide, 2018). The slip-weakening dependence of frictional strength (e.g., Ida, 1972) predicts that stable slip quasi-statically expands with time prior to the dynamic instability that leads to rupture. This feature is confirmed by in-situ experiments (Ohnaka & Kuwahara, 1990). Physical simulations indicate that interseismic creep penetrates seismogeneic patches from external stable-slip regions before the occurrence of unstable slip (Tse & Rice, 1986).

At present, it is difficult to determine the physics behind the observed hypocenter migration. However, our results suggest that aseismic phenomena preceded the 2017 Akita-Daisen earthquake.

Foreshock activity is sometimes reported to have significantly lower b-values than regular seismicity (e.g., Suyehiro, 1966; Enescu and Ito, 2001; Nanjo et al., 2012; Tormann et al., 2015; Tamarichuchi et al., 2018), which might be related to aseismic processes. In the case of the 2017 Akita-Daisen earthquake, we do not observe a significant change in b-value. The b-values of foreshocks and aftershocks are 0.90 and 0.93, respectively (Fig. S11). The standard errors for b-values are 0.13 for both foreshocks and aftershocks according to the solution of Shi & Bolt (1982).

5.2. Aftershock migration and afterslip propagation

One possible cause of the expansion of the aftershock region is the propagation of post-seismic aseismic slip (e.g., Wesson, 1987; Kato, 2004; Hsu et al., 2006; Ariyoshi et al., 2007). The expansion of aftershock region with the logarithm of time observed in this study is consistent with observations and simulations of post-seismic slip (Kato et al., 2007; Peng & Zhao, 2009; Frank et al., 2017; Perfettini et al., 2018; Ross et al., 2018). The propagation speed seems lower in the northern front than in the southern front (Fig. 9c). The difference in the propagation speed might be related to the difference in effective normal stress and/or frictional properties (Ariyoshi et al., 2007 and 2019). Some geodetic studies have showed that moment releases of post-seismic slip can be comparable to those of the mainshocks (Nishimura et al., 2000; Kawasaki et al., 2001; Pritchard & Simons, 2006; Freed, 2007; Johanson et al., 2006) especially for small to moderate-sized earthquakes (Hawthorne et al., 2016). This might suggest that the post-seismic slip also plays an important role for the release of stress in the case of this earthquake sequence.

Fluid diffusion is another possible cause for aftershock migration. However, hypocenter fronts expand with the square root of time in fluid diffusion models (e.g., Shapiro et al., 1997), which accurately describe the expansion of source regions of swarm activity, especially in volcanic regions (Parotidis et al., 2005; Yukutake et al., 2011a; Shelly et al., 2013a, 2013b, 2015; Yoshida et al., 2017, 2018). Our observation of aftershock expansion with the logarithm of time is better explained by the post-seismic slip propagation model.

Mainshock-aftershock sequences are characterized by a decay in the rate of seismicity in proportion to the reciprocal of time (Omori Law), and events are often assumed to be triggered by static stress changes from the mainshock (e.g., Dieterich, 1994; King et al., 1994) and/or post-seismic slip (e.g., Schaff et al., 1998; Hsu et al., 2006). On the other hand, earthquake swarms, which do not obey the Omori law, are often assumed to be caused by aseismic processes, such as episodic aseismic slip (Vidale & Shearer, 2006; Roland & McGuire, 2009; Chen et al., 2012) or fluid migration (e.g., Hainzl & Ogata, 2005). The number of aftershocks observed after the 2017 Akita-Daisen earthquake follows the Omori law (Fig. S12), which suggests that the dominant causes of these aftershocks were static stress change and post-seismic slip of the mainshock.

5.3. Spatial separation of co- and post-seismic slip, and foreshock and aftershock activities

We have suggested that the mainshock, foreshocks, and aftershocks released stress on different segments of the fault. Furthermore, aseismic slip probably influenced aftershock and foreshock generation, which also contributed to the redistribution of stress.

According to geodetic estimates, areas that undergo post-seismic slip are often spatially separated from those that experience coseismic slip (e.g., Heki et al., 1997; Miyazaki et al., 2004; Johanson et al., 2006; Miura et al., 2006 Wang et al., 2012; Iinuma et al., 2016), which may be attributed to variation in the frictional properties of faults. Fault segments on which post-seismic slip occurs are often modeled using velocity strengthening frictional behavior (e.g., Rice & Gu, 1983; Marone, 1991; Schaff et al., 1998; Perfettini & Avouac, 2004; Kato 2004; Viesca, 2019). In fact, post-seismic slip is often reported to occur at shallower and deeper levels than coseismic slip areas, which can be explained by the dependency of frictional properties on temperature (Tse & Rice, 1986; Blanpied et al., 1995). Post-seismic slip sometimes occurs at the same depth as coseismic slip (e.g., Hearn et al., 2002; Miyazaki et al., 2004; Hashimoto et al., 2006; Johnson et al., 2006; Hsu et al., 2006; Murakami et al., 2006; Pritchard & Simon, 2006; Uchida et al., 2009; Helmstetter & Shaw, 2009), which might reflect lateral variations in stress, frictional, and/or rheological properties along faults.

The spatial separation observed in this study may be attributable to differences in frictional properties along the fault; the areas with post-seismic slip might have a velocity-strengthening nature, but contain some small velocity-weakening patches on which aftershocks occurred. The rupture propagation of the mainshock may have been arrested by such a velocity-strengthening area. We usually do not know whether stable slip occurs along crustal faults at depth due to the weakness of the geodetic signal. However, the observation that fault segments characterized by velocity strengthening possibly exist may suggest that stable slip proceeds there during the interseismic period, and that slip deficit accumulates at other fault segments similar to the processes characteristic of plate boundary faults.

Aftershocks did not occur in the area between the two large slip regions and deeper portions ($z > 10$ km) even if the shear stress magnitude was increased by the mainshock (Fig. 12). This may indicate that shear stress was released aseismically rather than through aftershock generation.

5.2. Stress release processes along the fault of the Akita-Daisen earthquake

The temporal evolution of stress associated the Akita-Daisen earthquake can be summarized as follows:

(1) Shear stress along the fault continuously increased following the 2011 Tohoku-Oki earthquake due to coseismic and postseismic deformation.

(2) Seismicity drastically increased after the 2011 Tohoku-Oki earthquake in and around the focal region. Foreshocks started to occur ~2,000 days before the mainshock, and their hypocenters migrated along the fault plane from north to south, redistributing shear stress on the fault. We suspect that aseismic slip was responsible for foreshock activity, which also contributed to the redistribution of stress on the fault.

(3) The M5.2 mainshock finally occurred six years after the 2011 Tohoku-Oki earthquake and primary propagated toward the north. The mainshock released shear stress accumulated on

some segments of the fault (stress drop of 1.4 MPa on average). The amount of coseismic slip was smaller in areas where foreshocks had already released stress. Heterogeneous states of stress and/or friction may have contributed to the heterogeneous distribution of coseismic slip. The mainshock increased shear stress near the edges of large slip regions.

(4) Aftershocks occurred abundantly in areas where shear stress was increased by the mainshock. The aftershock region expanded along the fault strike, probably associated with the propagation of postseismic slip.

6. Discussion

6.1. Possible repeating earthquakes along the crustal fault and estimation of postseismic slip magnitude

Repeating earthquakes, i.e., those which repeatedly cause slip on the same portion of a fault, have been used to examine the occurrence and characteristics of aseismic slip along plate boundaries (e.g., Ellsworth, 1995; Nadeau & McEbilly, 1999; Igarashi et al., 2003; Uchida et al., 2003, 2004; Uchida & Matsuzawa, 2013). Recently, repeating earthquakes have also been detected along crustal faults (Bourouis & Bernard, 2007; Hiramatsu et al., 2011; Hayashi & Hiramatsu, 2013; Naoi et al., 2015), and it is anticipated they may help to investigate aseismic phenomena (Uchida & Bürgman).

Fig. 5 shows that several M~3 earthquakes occur very close to the southern front of the aftershock area (gray rectangle). Fig. 13 shows an enlarged view of the southern portion of the aftershock area. Two earthquakes of M2.6 and M2.9 in cross-section B, at a depth of about 1.4 km, lie very close to each other (23 m). Similarly, two earthquakes of M3.0 and M3.2 in cross-section C, at a depth of about 1.4 km, are very close to each other (41 m). We call these two earthquake pairs possible repeating earthquake pair #1 and #2, respectively.

The earthquakes possibly caused slip on the same portions of the fault. Their magnitudes are relatively large at about M3, and their locations are very close to each other compared with their fault sizes (360 and 240 m for stress drop of 3 and 10 MPa, respectively). Their distances apart are a few tens of meters, which are much shorter than the fault sizes based on the crack model. Figs. 13 (c) and (d) show the uncertainty in the relative distances of the two possible repeating earthquake pairs obtained by the 1,000 bootstrap hypocenter relocations. In most results, their distances are estimated to be less than 50 m, which is much smaller than the expected source sizes. They occur in the hypocenter expansion front, which is consistent with the hypothesis that they are caused by post-seismic slip propagation.

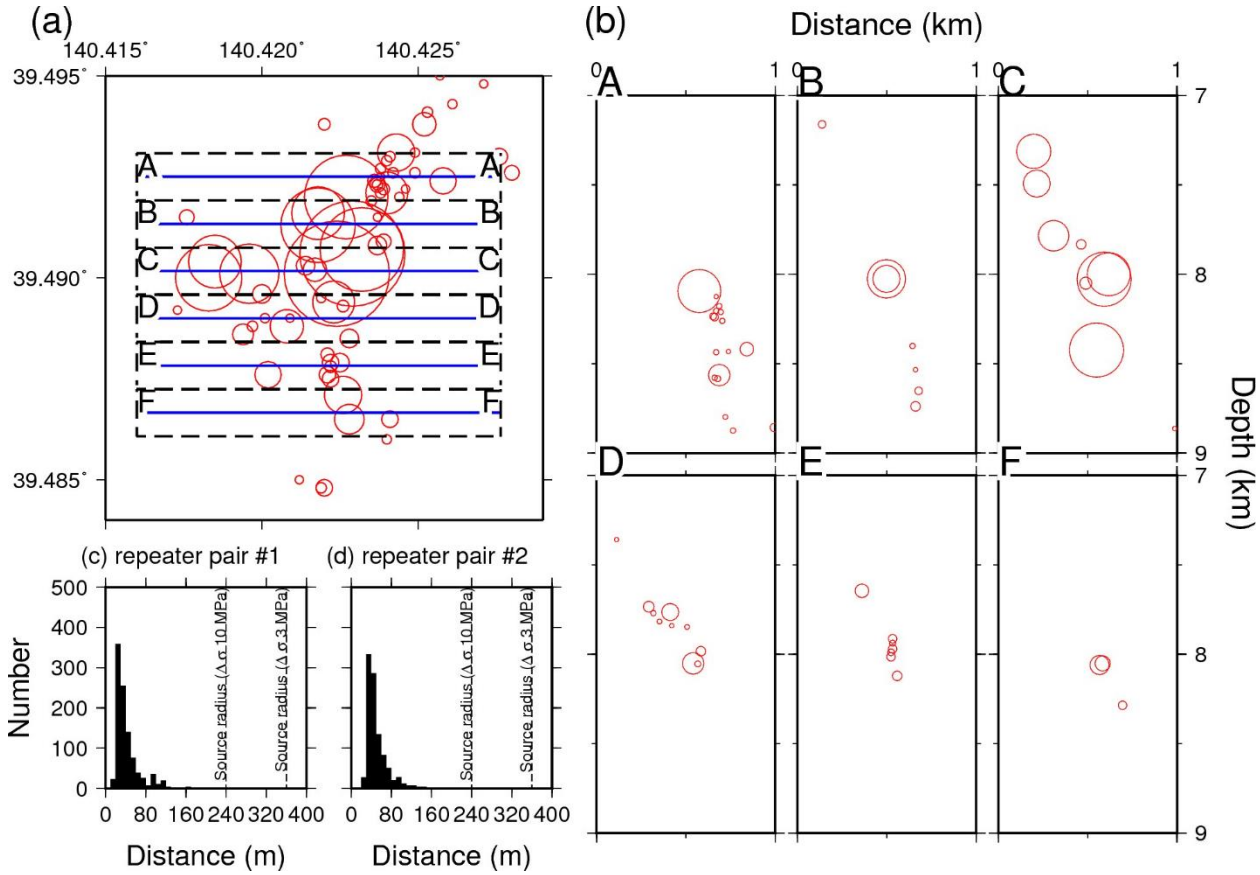

Fig. 13. (a) Enlarged map view, and (b) cross-sectional views across the fault strike showing the hypocenters of aftershocks (circles). Repeating earthquakes can be observed in cross sections B and C. The location is outlined in Fig. 5 by the gray rectangle. The size of each circle corresponds to the fault diameter, assuming a stress drop of 10 MPa. (c), (d) Uncertainty in the distances between the two sets of possible repeating earthquakes obtained by 1,000 relocation iterations, based on bootstrap subsampling of (c) possible repeating earthquake pair #1 and (d) possible repeating earthquake pair #2.

The locations of these earthquakes are similar but slightly different (a few tens of meters). Example waveforms of these four earthquakes at the nearest seismic station are similar but not identical (Fig. S13). The different waveforms suggest that these earthquakes caused slip on the same portion on the fault, but the rupture processes were different. Such a difference in rupture processes and waveforms of repeating earthquakes is also observed for interplate repeating earthquakes (Shimamura et al., 2012).

6.2. Stress release process along crustal fault

The 2017 M5.2 Akita-Daisen earthquake sequence occurred on a crustal fault, but has similar features to interplate earthquakes. For example, in the case of the 2011 M9 Tohoku-Oki earthquake, the spatial distribution of aftershocks shows a clear seismic gap corresponding to the

large mainshock coseismic slip region (e.g., Asano et al., 2011; Kato & Igarashi, 2012; Nakamura et al., 2016). Foreshock hypocenters migrated to the rupture initiation point of the mainshock, which was interpreted as the propagation of aseismic slip (Ando & Imanishi, 2011; Kato et al., 2012). The aftershock region expanded with the logarithm of time, which was attributed to post-seismic aseismic slip of the mainshock (Lengline et al., 2011; Perfettini et al., 2018). During the post-seismic period, earthquakes repeatedly occurred on the same portions of the fault, and were probably triggered by aseismic slip (Uchida & Matsuzawa, 2013). Overall, the foreshocks, mainshock, aftershocks, and post-seismic slip all released stress at different fault segments in the M9 event (Hasegawa & Yoshida, 2015; Iinuma et al., 2016). These features of the megathrust earthquake are similar to those observed for the M5 intraplate earthquake in this study. These similarities are consistent with the hypothesis that the process of stress release along crustal faults is essentially the same as that along plate boundaries.

In this study, we focused on an M5 earthquake sequence that occurred on a single fault plane. Fault structures in the crust, however, are usually more complex, and their interactions play important roles in the three-dimensional release of stress in the crust (Urata et al., 2017). When faults are randomly distributed in space, shear strain energy density can be a measure of the average shear stress over the faults (Saito et al., 2018). Recent studies reported that the change of shear strain energy density affects seismicity in the seismogeneic zone (Noda et al., 2020; Terakawa et al., 2020). To improve our understanding of the deformation process in the crust, future work should consider the interactions of complex fault distributions.

6.3. Constraints on absolute stress magnitude in NE Japan

Drastic changes in focal mechanisms were observed after the 2011 M9 Tohoku-Oki earthquake across a large part of east Japan, from the off-shore source region (Asano et al., 2011) to inland areas a few hundred kilometers from the source region (Kato et al., 2011; Yoshida et al., 2012). Stress fields were estimated to have rotated by > 30° after this earthquake (e.g., Hasegawa et al., 2011 and 2012; Hardebeck, 2012; Yoshida et al., 2012). Differential stress magnitudes estimated from the rotation of stress fields are about 20 MPa near the source region (Hasegawa et al., 2012) and as small as 1 MPa in and around the source region of the Akita-Daisen earthquake (Yoshida et al., 2012). This suggests that fault weakening mechanisms, such as drastic increases in pore pressure, play important roles in the occurrence of earthquakes (e.g., Rice, 1992; Sibson, 1992). On the other hand, stress orientations estimated by seismological methods can be biased due to the existence of strong heterogeneity in stress fields, which can lead to a large underestimation of deviatoric stress magnitudes (Smith & Dieterich, 2010; Smith & Heaton, 2011).To improve our understanding of deformation processes in the earth, it is important to confirm whether earthquakes occur under such very low shear stresses or not. The source process of the M5.2 earthquake provides a clue as to whether the absolute stress magnitude in NE Japan is truly very small (< 1 MPa), and whether strength reduction mechanisms are controlling factors for the occurrence of earthquakes.

Earthquakes occur to release strain energy stored in the crust. The change in strain energy associated with a stress drop of $\Delta\sigma$ is

$$\Delta E = -\frac{M_0}{2\mu}(2\tau_0 - \Delta\sigma) \quad (3)$$

where τ_0 is initial stress (e.g., Aki & Richards. 2002). The radiation energy is a part of the released strain energy, so $-\Delta E > E_r$. Therefore,

$$\tau_0 > \frac{\Delta\sigma}{2} + \mu\frac{E_r}{M_o} = \frac{\Delta\sigma}{2} + \sigma_{ap} \quad (4)$$

This relationship is valid regardless of assumptions regarding frictional constitutive laws. If we substitute $\Delta\tau = 1.4$ MPa and $\sigma_{ap} = 0.5$ MPa, we obtain $\tau_0 > 1.2$ MPa. Moreover, the stress drop is underestimated if the short-wavelength components are underestimated in the slip distribution (Saito & Noda 2019). In this case, the initial stress required to excite the earthquake faulting would be larger. Therefore, the initial stress must be larger than 1.2 MPa. This is significantly higher than the 0.5 MPa maximum shear stress magnitude that can reproduce the observed rotations of the principal stress orientations after the 2011 Tohoku-Oki earthquake (Yoshida et al., 2012). The rupture process of the 2017 M5.2 Akita-Daisen earthquake therefore indicates that the stress orientations in inland NE Japan did not rotate after the 2011 Tohoku-Oki earthquake. The apparent stress rotation probably comes from spatial heterogeneity in the stress fields (Yoshida et al., 2019). This was partly supported by a relatively high radiation efficiency of this earthquake, which suggests that the fault which caused the 2017 M5.2 earthquake may have slipped repeatedly, and its stress field remains constant for time periods longer than the 6 years which have elapsed since the 2011 Tohoku-Oki earthquake.

7. Conclusions

Stress accumulation and release processes in the crust are poorly understood compared to those at plate boundaries. The weakness of the geodetic signal of aseismic slip at crustal faults, and the complexity of crustal fault structure in the crust, restrict our understanding. This study examined foreshock and aftershock activities of the 2017 M5.2 Akita-Daisen earthquake, which has a simple fault geometry, to extract information about the processes of stress accumulation and release in the crust.

We relocated the hypocenters of 554 $M_{JMA} \geq 1$ earthquakes for the period 2003–2018 in the rupture area of the M5.2 mainshock using the waveform cross-correlation technique, and determined their focal mechanisms. We also determined the moment rate function of the mainshock and estimated the source process based on the waveform inversion method.

Relocated hypocenters indicated that hypocenters were concentrated on a planar structure with N-S strike which dips eastward at a high angle, consistent with their focal mechanisms. Furthermore, foreshocks, the mainshock, and aftershocks occurred on different fault segments and released stress in a complementary manner.

Hypocenters of foreshocks migrated from the northern to the southern part of the rupture area, which suggests that the M5.2 earthquake and aftershocks were triggered by aseismic phenomena, such as fluid migration and episodic aseismic slip. Foreshock migration may be caused by the quasi-static expansion of stable slip associated with nucleation of the mainshock.

Abundant aftershocks occurred near the edge of large coseismic slip regions, on which shear stress increased after the earthquake. The aftershock region expanded along the fault strike with the logarithm of time, which can be attributed to post-seismic aseismic slip of the mainshock. During the post-seismic period, possible repeating earthquakes (~M3) occurred on the same portions of the fault, which may be triggered by aseismic slip.

Areas with coseismic slip are spatially separated from those with post-seismic slip (estimated from aftershock migration), which might reflect differences in frictional properties. The areas with post-seismic slip may be of a velocity-strengthening nature, but contain some small velocity-weakening patches on which aftershocks occurred. Rupture propagation of the mainshock may have been inhibited by velocity strengthening areas. This suggests that some portions of the fault creep during the interseismic period. These features are similar to those of megathrust earthquakes, which suggests that the stress release processes along crustal faults are not essentially different from those along plate boundaries.

Acknowledgments

We deeply thank the editor and two anonymous reviewers for their constructive comments, which helped to improve the manuscript. KY thanks Akira Hasegawa for discussions about repeating earthquakes and post-seismic slip, and Hisahiko Kubo for discussions about waveform inversion. This study used hypocenters and P-and S-wave arrival time data reported in the unified catalog of the JMA (https://www.data.jma.go.jp/svd/eqev/data/bulletin/hypo_e.html). The seismograms were collected and stored by JMA, national universities, and National Research Institute for Earth Science and Disaster Resilience (http://www.hinet.bosai.go.jp/?LANG=en). The figures in this paper were created using GMT (Wessel and Smith, 1998). Obtained results of hypocenters, focal mechanisms, and coseismic slip distribution are available at http://www.aob.gp.tohoku.ac.jp/~yoshida/pub/JGR2020/.

References

Aki, K., & Richards, P. G. (2002). Quantitative seismology. https://doi.org/10.1016/S0065-230X(09)04001-9

Ando, R., & Imanishi, K. (2011). Possibility of M w 9.0 mainshock triggered by diffusional propagation of after-slip from M w 7.3 foreshock. Earth, Planets and Space, 63(7), 767–771. https://doi.org/10.5047/eps.2011.05.016

Ando, R., Nakata, R., & Hori, T. (2010). A slip pulse model with fault heterogeneity for low-frequency earthquakes and tremor along plate interfaces. Geophysical Research Letters, 37(10).

Ariyoshi, K., Matsuzawa, T., & Hasegawa, A. (2007). The key frictional parameters controlling spatial variations in the speed of postseismic-slip propagation on a subduction plate boundary. Earth and Planetary Science Letters, 256(1–2), 136–146.

Ariyoshi, K., Ampuero, J.-P., Bürgmann, R., Matsuzawa, T., Hasegawa, A., Hino, R., & Hori, T. (2019). Quantitative relationship between aseismic slip propagation speed and frictional properties. Tectonophysics, 767, 128151.

Asano, Y., Saito, T., Ito, Y., Shiomi, K., Hirose, H., Matsumoto, T., et al. (2011). Spatial distribution and focal mechanisms of aftershocks of the 2011 off the Pacific coast of Tohoku Earthquake. Earth, Planets and Space, 63(7), 29.

Asanuma, H., Ishimoto, M., Jones, R. H., Phillips, W. S., & Niitsuma, H. (2001). A variation of the collapsing method to delineate structures inside a microseismic cloud. Bulletin of the Seismological Society of America, 91(1), 154–160. https://doi.org/10.1785/0120000063

Beeler, N. M., Lockner, D. L., & Hickman, S. H. (2001). A simple stick-slip and creep-slip model for repeating earthquakes and its implication for microearthquakes at Parkfield. Bulletin of the Seismological Society of America, 91(6), 1797–1804.

Beroza, G. C., & Ide, S. (2011). Slow earthquakes and nonvolcanic tremor. Annual Review of Earth and Planetary Sciences, 39, 271–296.

Blanpied, M. L., Lockner, D. A., & Byerlee, J. D. (1995). Frictional slip of granite at hydrothermal conditions. Journal of Geophysical Research: Solid Earth, 100(B7), 13045–13064.

Bourouis, S., & Bernard, P. (2007). Evidence for coupled seismic and aseismic fault slip during water injection in the geothermal site of Soultz (France), and implications for seismogenic transients. Geophysical Journal International, 169(2), 723–732.

Chen, X., Shearer, P. M., & Abercrombie, R. E. (2012). Spatial migration of earthquakes within seismic clusters in Southern California: Evidence for fluid diffusion. Journal of Geophysical Research: Solid Earth, 117(4), 1–7. https://doi.org/10.1029/2011JB008973

Dahm, T. (1996). Relative moment tensor inversion based on ray theory: theory and synthetic tests. Geophysical Journal International, 124(1), 245–257.

Das, S., & Henry, C. (2003). Spatial relation between main earthquake slip and its aftershock distribution. Reviews of Geophysics, 41(3).

Dodge, D. A., Beroza, G. C., & Ellsworth, W. L. (1996). Detailed observations of California foreshock sequences: Implications for the earthquake initiation process. Journal of Geophysical Research: Solid Earth, 101(B10), 22371–22392.

Ebel, J. E., & Chambers, D. W. (2016). Using the locations of M≥ 4 earthquakes to delineate the extents of the ruptures of past major earthquakes. Geophysical Supplements to the Monthly Notices of the Royal Astronomical Society, 207(2), 862–875.

Frank, W. B., Poli, P., & Perfettini, H. (2017). Mapping the rheology of the Central Chile subduction zone with aftershocks. Geophysical Research Letters, 44(11), 5374–5382.

Freund, L. B. (1972). Crack propagation in an elastic solid subjected to general loading—I. Constant rate of extension. Journal of the Mechanics and Physics of Solids, 20(3), 129–140.

Fukuyama, E. (1998). Automated seismic moment tensor determination by using on-line broadband seismic wave-forms. Zisin 2, 51, 149–156.

Geller, R. J. (1976). SCALING RELATIONS FOR EARTHQUAKE SOURCE PARAMETERS AND MAGNITUDES. Bulletin of the Seismological Society of America (Vol. 66).

Hainzl, S., & Ogata, Y. (2005). Detecting fluid signals in seismicity data through statistical earthquake modeling. Journal of Geophysical Research: Solid Earth, 110(5), 1–10. https://doi.org/10.1029/2004JB003247

Hartzell, B. Y. S. H., & Heaton, T. H. (1983). INVERSION OF STRONG GROUND MOTION AND TELESEISMIC WAVEFORM DATA FOR THE FAULT RUPTURE HISTORY OF THE 1979 IMPERIAL VALLEY, CALIFORNIA, EARTHQUAKE. Bulletin of the Seismological Society of America, 73(6), 1553–1583.

Hartzell, S. H. (1978). Earthquakes aftershocks as Green's Functions. Geophysical Research Letters, 5(1), 1–4. https://doi.org/10.1029/GL005i001p00001

Hasegawa, A., Umino, N., & Takagi, A. (1978). Double-planed structure of the deep seismic zone in the northeastern Japan arc. Tectonophysics, 47(1–2), 43–58. https://doi.org/10.1016/0040-1951(78)90150-6

Hashimoto, C., Noda, A., Sagiya, T., & Matsu'ura, M. (2009). Interplate seismogenic zones along the Kuril--Japan trench inferred from GPS data inversion. Nature Geoscience, 2(2), 141.

Hawthorne, J. C., Simons, M., & Ampuero, J.-P. (2016). Estimates of aseismic slip associated with small earthquakes near San Juan Bautista, CA. Journal of Geophysical Research: Solid Earth, 121(11), 8254–8275.

Hayashi, M., & Hiramatsu, Y. (2013). Spatial distribution of similar aftershocks of a large inland earthquake, the 2000 Western Tottori earthquake, in Japan. Earth, Planets and Space, 65(12), 1587–1592.

Hearn, E. H., Bürgmann, R., & Reilinger, R. E. (2002). Dynamics of Izmit earthquake postseismic deformation and loading of the Duzce earthquake hypocenter. Bulletin of the Seismological Society of America, 92(1), 172–193.

Heki, K., Miyazaki, S., & Tsuji, H. (1997). Silent fault slip following an interplate thrust earthquake at the Japan Trench. Nature, 386(6625), 595.

Helmstetter, A., & Shaw, B. E. (2009). Afterslip and aftershocks in the rate-and-state friction law. Journal of Geophysical Research: Solid Earth, 114(1). https://doi.org/10.1029/2007JB005077

Henry, C., & Das, S. (2001). Aftershock zones of large shallow earthquakes: fault dimensions, aftershock area expansion and scaling relations. Geophysical Journal International, 147(2), 272–293.

Hiramatsu, Y., Hayashi, M., & Hayashi, A. (2011). Relation between similar aftershocks and ruptured asperity of a large inland earthquake: Example of the 2007 Noto Hanto earthquake. Earth, Planets and Space, 63(2), 145.

Hirose, H., Hirahara, K., Kimata, F., Fujii, N., & Miyazaki, S. (1999). A slow thrust slip event following the two 1996 Hyuganada earthquakes beneath the Bungo Channel, southwest Japan. Geophysical Research Letters, 26(21), 3237–3240.

Hsu, Y. J., Simons, M., Avouac, J. P., Galeteka, J., Sieh, K., Chlieh, M., et al. (2006). Frictional afterslip following the 2005 Nias-Simeulue earthquake, Sumatra. Science. https://doi.org/10.1126/science.1126960

Ida, Y. (1972). Cohesive force across the tip of a longitudinal-shear crack and Griffith's specific surface energy. Journal of Geophysical Research, 77(20), 3796–3805.

Ide, S., Beroza, G. C., Shelly, D. R., & Uchide, T. (2007). A scaling law for slow earthquakes. Nature, 447(7140), 76–79. https://doi.org/10.1038/nature05780

Igarashi, T., Matsuzawa, T., & Hasegawa, A. (2003). Repeating earthquakes and interplate aseismic slip in the northeastern Japan subduction zone. Journal of Geophysical Research: Solid Earth, 108(B5).

Iinuma, T., Hino, R., Uchida, N., Nakamura, W., Kido, M., Osada, Y., & Miura, S. (2016). Seafloor observations indicate spatial separation of coseismic and postseismic slips in the 2011 Tohoku earthquake. Nature Communications, 7, 13506.

Iinuma, T., Ohzono, M., Ohta, Y., & Miura, S. (2011). Coseismic slip distribution of the 2011 off the Pacific coast of Tohoku Earthquake (M 9.0) estimated based on GPS data—Was the asperity in Miyagi-oki ruptured? Earth, Planets and Space, 63(7), 24.

Iio, Y., Sagiya, T., Kobayashi, Y., & Shiozaki, I. (2002). Water-weakened lower crust and its role in the concentrated deformation in the Japanese Islands. Earth and Planetary Science Letters, 203(1), 245–253.

Johanson, I. A., Fielding, E. J., Rolandone, F., & Bürgmann, R. (2006). Coseismic and postseismic slip of the 2004 Parkfield earthquake from space-geodetic data. Bulletin of the Seismological Society of America, 96(4B), S269--S282.

Kagan, Y. Y. (1991). 3-D rotation of double-couple earthquake sources. Geophysical Journal International, 106(3), 709–716.

Kanamori, H., & Rivera, L. (2006). Energy partitioning during an earthquake.

Kato, A., & Igarashi, T. (2012). Regional extent of the large coseismic slip zone of the 2011 Mw 9.0 Tohoku-Oki earthquake delineated by on-fault aftershocks. Geophysical Research Letters, 39(15).

Kato, A., Obara, K., Igarashi, T., Tsuruoka, H., Nakagawa, S., & Hirata, N. (2012). Propagation of slow slip leading up to the 2011 Mw 9.0 Tohoku-Oki earthquake. Science, 335(6069), 705–708.

Kato, A., Sakai, S., & Obara, K. (2011). A normal-faulting seismic sequence triggered by the 2011 off the Pacific coast of Tohoku Earthquake: Wholesale stress regime changes in the upper plate. Earth, Planets and Space, 63(7), 745–748. https://doi.org/10.5047/eps.2011.06.014

Kato, N. (2004). Interaction of slip on asperities: Numerical simulation of seismic cycles on a two-dimensional planar fault with nonuniform frictional property. Journal of Geophysical Research: Solid Earth, 109(B12).

Kato, N. (2007). Expansion of aftershock areas caused by propagating post-seismic sliding. Geophysical Journal International, 168(2), 797–808.

Kawasaki, I., Asai, Y., & Tamura, Y. (2001). Space-time distribution of interplate moment release including slow earthquakes and the seismo-geodetic coupling in the Sanriku-oki region along the Japan trench. Tectonophysics, 330, 267–283. https://doi.org/10.1016/S0040-1951(00)00245-6

Kilb, D., & Rubin, A. M. (2002). Implications of diverse fault orientations imaged in relocated aftershocks of the Mount Lewis, M L 5.7, California, earthquake. Journal of Geophysical Research: Solid Earth, 107(B11), ESE 5-1-ESE 5-17. https://doi.org/10.1029/2001jb000149

King, G. C. P., Stein, R. S., & Lin, J. (1994). Static stress changes and the triggering of earthquakes. Bulletin of the Seismological Society of America, 84(3), 935–953.

Knopoff, L. (1958). Energy Release in Earthquakes. Geophysical Journal of the Royal Astronomical Society, 1(1), 44–52. https://doi.org/10.1111/j.1365-246X.1958.tb00033.x

Lawson, C. L., & Hanson, R. J. (1995). Solving least squares problems (Vol. 15). Siam.

Lay, T., Ammon, C. J., Hutko, A. R., & Kanamori, H. (2010). Effects of kinematic constraints on teleseismic finite-source rupture inversions: Great Peruvian earthquakes of 23 June 2001 and 15 August 2007. Bulletin of the Seismological Society of America, 100(3), 969–994.

Lay, T., & Kanamori, H. (1981). An asperity model of large earthquake sequences. In Earthquake Prediction. Maurice Ewing Series (pp. 579–592). American Geophysical Union.

Lengliné, O., Enescu, B., Peng, Z., & Shiomi, K. (2012). Decay and expansion of the early aftershock activity following the 2011, Mw9. 0 Tohoku earthquake. Geophysical Research Letters, 39(18).

Ligorría, J. P., & Ammon, C. J. (1999). Iterative deconvolution and receiver-function estimation. Bulletin of the Seismological Society of America, 89(5), 1395–1400. https://doi.org/10.1016/S0304-3940(97)00816-1

Linde, A. T., Gladwin, M. T., Johnston, M. J. S., Gwyther, R. L., & Bilham, R. G. (1996). A slow earthquake sequence on the San Andreas fault. Nature, 383(6595), 65.

Liu, Y., & Rice, J. R. (2005). Aseismic slip transients emerge spontaneously in three-dimensional rate and state modeling of subduction earthquake sequences. Journal of Geophysical Research: Solid Earth, 110(B8).

Lohman, R. B., & McGuire, J. J. (2007). Earthquake swarms driven by aseismic creep in the Salton Trough, California. Journal of Geophysical Research: Solid Earth. https://doi.org/10.1029/2006JB004596

Marone, C. J., Scholtz, C. H., & Bilham, R. (1991). On the mechanics of earthquake afterslip. Journal of Geophysical Research: Solid Earth, 96(B5), 8441–8452.

Masayuki Kikuchi, and H. K. (1982). Inversion of complex body waves. Bulletin of the Seismological Society of America, 72(2), 491–506.

Matsu'ura, M., Kataoka, H., & Shibazaki, B. (1992). Slip-dependent friction law and nucleation processes in earthquake rupture. Tectonophysics, 211(1–4), 135–148.

Matsu'ura, M., & Sato, T. (1989). A dislocation model for the earthquake cycle at convergent plate boundaries. Geophysical Journal International, 96(1), 23–32.

Matsuzawa, T., Igarashi, T., & Hasegawa, A. (2002). Characteristic small-earthquake sequence off Sanriku, northeastern Honshu, Japan. Geophysical Research Letters, 29(11), 38.

McGuire, J. J., Boettcher, M. S., & Jordan, T. H. (2005). Foreshock sequences and short-term earthquake predictability on East Pacific Rise transform faults. Nature, 434(7032), 457.

McGuire, J. J., & Jordan, T. H. (2000). Further evidence for the compound nature of slow earthquakes: The Prince Edward Island earthquake of April 28, 1997. Journal of Geophysical Research: Solid Earth, 105(B4), 7819–7827.

Meneses-Gutierrez, A., & Sagiya, T. (2016). Persistent inelastic deformation in central Japan revealed by GPS observation before and after the Tohoku-oki earthquake. Earth and Planetary Science Letters, 450, 366–371.

Mendoza, C., & Hartzell, S. H. (1988). Aftershock patterns and main shock faulting. Bulletin of the Seismological Society of America, 78(4), 1438–1449.

Miura, S., Iinuma, T., Yui, S., Uchida, N., Sato, T., Tachibana, K., & Hasegawa, A. (2006). Co- and post-seismic slip associated with the 2005 Miyagi-oki earthquake (M7. 2) as inferred from GPS data. Earth, Planets and Space, 58(12), 1567–1572.

Miyazaki, S., Segall, P., Fukuda, J., & Kato, T. (2004). Space time distribution of afterslip following the 2003 Tokachi-oki earthquake: Implications for variations in fault zone frictional properties. Geophysical Research Letters, 31(6).

Mogi, K. (1969). 18. Relationship between the Occurrence of Great Earthquakes and Tectonic Structures.

Moriya, H., Fujita, T., Niitsuma, H., Eisenblätter, J., & Manthei, G. (2006). Analysis of fracture propagation behavior using hydraulically induced acoustic emissions in the Bernburg salt mine, Germany. International Journal of Rock Mechanics and Mining Sciences, 43(1), 49–57. https://doi.org/10.1016/j.ijrmms.2005.04.003

Murakami, M., Suito, H., Ozawa, S., & Kaidzu, M. (2006). Earthquake triggering by migrating slow slip initiated by M8 earthquake along Kuril Trench, Japan. Geophysical Research Letters, 33(9).

Nakamura, W., Uchida, N., & Matsuzawa, T. (2016). Spatial distribution of the faulting types of small earthquakes around the 2011 Tohoku-oki earthquake: A comprehensive search using template events. Journal of Geophysical Research: Solid Earth, 121(4), 2591–2607.

Nanjo, K. Z., Hirata, N., Obara, K., & Kasahara, K. (2012). Decade-scale decrease inb value prior to the M9-class 2011 Tohoku and 2004 Sumatra quakes. Geophysical Research Letters, 39(20).

Nishimura, T., Miura, S., Tachibana, K., Hashimoto, K., Sato, T., Hori, S., et al. (2000). Distribution of seismic coupling on the subducting plate boundary in northeastern Japan inferred from GPS observations. Tectonophysics, 323(3–4), 217–238.

Noda, A., Saito, T., & Fukuyama, E. (2018). Slip-Deficit Rate Distribution Along the Nankai Trough, Southwest Japan, With Elastic Lithosphere and Viscoelastic Asthenosphere. Journal of Geophysical Research: Solid Earth, 123(9), 8125–8142.

Noda, A., Saito, T., Fukuyama, E., Terakawa, T., Tanaka, S., & Matsu'ura, M. 3-D Spatial Distribution of Shear Strain Energy Changes Associated with the 2016 Kumamoto Earthquake Sequence, Southwest Japan. Geophysical Research Letters, e2019GL086369.

Noda, H., Lapusta, N., & Kanamori, H. (2013). Comparison of average stress drop measures for ruptures with heterogeneous stress change and implications for earthquake physics. Geophysical Journal International, 193(3), 1691–1712.

Ohnaka, M., & Kuwahara, Y. (1990). Characteristic features of local breakdown near a crack-tip in the transition zone from nucleation to unstable rupture during stick-slip shear failure. Tectonophysics, 175(1–3), 197–220.

Okada, T., Matsuzawa, T., Umino, N., Yoshida, K., Hasegawa, A., Takahashi, H., et al. (2016). Hypocenter migration and crustal seismic velocity distribution observed for the inland earthquake swarms induced by the 2011 Tohoku-Oki earthquake in NE Japan: Implications for crustal fluid distribution and crustal permeability. In Crustal Permeability. https://doi.org/10.1002/9781119166573.ch24

Okada, Y. (1992). INTERNAL DEFORMATION DUE TO SHEAR AND TENSILE FAULTS IN A HALF-SPACE. Bulletin of the Geological Society of America, 82(2), 1018–1040. https://doi.org/10.1029/92JB00178

Parotidis, M., Rothert, E., & Shapiro, S. A. (2003). Pore-pressure diffusion: A possible triggering mechanism for the earthquake swarms 2000 in Vogtland/NW-Bohemia, central Europe. Geophysical Research Letters, 30(20), n/a-n/a. https://doi.org/10.1029/2003GL018110

Peng, Z., & Zhao, P. (2009). Migration of early aftershocks following the 2004 Parkfield earthquake. Nature Geoscience, 2(12), 877.

Perfettini, H., & Avouac, J.-P. (2004). Postseismic relaxation driven by brittle creep: A possible mechanism to reconcile geodetic measurements and the decay rate of aftershocks, application to the Chi-Chi earthquake, Taiwan. Journal of Geophysical Research: Solid Earth, 109(B2).

Perfettini, H., Frank, W. B., Marsan, D., & Bouchon, M. (2018). A model of aftershock migration driven by afterslip. Geophysical Research Letters, 45(5), 2283–2293.

Pritchard, M. E., & Simons, M. (2006). An aseismic slip pulse in northern Chile and along-strike variations in seismogenic behavior. Journal of Geophysical Research: Solid Earth, 111(B8).

Rice, J. R. (1992). Fault stress states, pore pressure distributions, and the weakness of the San Andreas fault. In International geophysics (Vol. 51, pp. 475–503). Elsevier.

Rice, J. R., & Gu, J. (1983). Earthquake aftereffects and triggered seismic phenomena. Pure and Applied Geophysics, 121(2), 187–219.

Roland, E., & McGuire, J. J. (2009). Earthquake swarms on transform faults. Geophysical Journal International, 178(3), 1677–1690. https://doi.org/10.1111/j.1365-246X.2009.04214.x

Ross, Z. E., Hauksson, E., & Ben-Zion, Y. (2017a). Abundant off-fault seismicity and orthogonal structures in the San Jacinto fault zone. Science Advances, 3(3), e1601946.

Ross, Z. E., Kanamori, H., & Hauksson, E. (2017b). Anomalously large complete stress drop during the 2016 Mw5.2 Borrego Springs earthquake inferred by waveform modeling and near-source aftershock deficit. Geophysical Research Letters, 44(12), 5994–6001. https://doi.org/10.1002/2017GL073338

Ross, Z. E., Kanamori, H., Hauksson, E., & Aso, N. (2018). Dissipative Intraplate Faulting During the 2016 Mw6.2 Tottori, Japan Earthquake. Journal of Geophysical Research: Solid Earth, 123(2), 1631–1642. https://doi.org/10.1002/2017JB015077

Ross, Z. E., Idini, B., Jia, Z., Stephenson, O. L., Zhong, M., Wang, X., … others. (2019). Hierarchical interlocked orthogonal faulting in the 2019 Ridgecrest earthquake sequence. Science, 366(6463), 346–351.

Ryder, I., & Bürgmann, R. (2008). Spatial variations in slip deficit on the central San Andreas fault from InSAR. Geophysical Journal International, 175(3), 837–852.

Saito, T., Noda, A., Yoshida, K., & Tanaka, S. (2018). Shear Strain Energy Change Caused by the Interplate Coupling Along the Nankai Trough: An Integration Analysis Using Stress Tensor Inversion and Slip-Deficit Inversion. Journal of Geophysical Research: Solid Earth, 123(7), 5975–5986.

Saito, T., & Noda, A. (2020). Strain energy released by earthquake faulting with random slip components. Geophysical Journal International, 220(3), 2009-2020.

Savage, J. C. (1969). Steketee's paradox. Bulletin of the Seismological Society of America, 59(1), 381–384.

Savage, J. C. (1983). A dislocation model of strain accumulation and release at a subduction zone. Journal of Geophysical Research: Solid Earth, 88(B6), 4984–4996.

Schaff, D. P., Beroza, G. C., & Shaw, B. E. (1998). Postseismic response of repeating aftershocks. Geophysical Research Letters, 25(24), 4549–4552.

1036 Shao, G., Ji, C., & Hauksson, E. (2012). Rupture process and energy budget of the 29 July 2008
1037 Mw 5.4 Chino Hills, California, earthquake. Journal of Geophysical Research: Solid
1038 Earth, 117(B7).

1039 Shapiro, S. A., Huenges, E., & Borm, G. (1997). Estimating the crust permeability from fluid-
1040 injection-induced seismic emission at the KTB site. Geophysical Journal International,
1041 131(2). https://doi.org/10.1111/j.1365-246X.1997.tb01215.x

1042 Shelly, D. R., Hill, D. P., Massin, F., Farrell, J., Smith, R. B., & Taira, T. (2013). A fluid-driven
1043 earthquake swarm on the margin of the Yellowstone caldera. Journal of Geophysical
1044 Research E: Planets, 118(9), 4872–4886. https://doi.org/10.1002/jgrb.50362

1045 Shelly, D. R., Moran, S. C., & Thelen, W. A. (2013). Evidence for fluid-triggered slip in the
1046 2009 Mount Rainier, Washington earthquake swarm. Geophysical Research Letters,
1047 40(8), 1506–1512. https://doi.org/10.1002/grl.50354

1048 Shelly, D. R., Taira, T., Prejean, S. G., Hill, D. P., & Dreger, D. S. (2015). Fluid-faulting
1049 interactions: Fracture-mesh and fault-valve behavior in the February 2014 Mammoth
1050 Mountain, California, earthquake swarm. Geophysical Research Letters, 42(14), 5803–
1051 5812. https://doi.org/10.1002/2015GL064325

1052 Shi, Y., & Bolt, B. A. (1982). THE STANDARD ERROR OF THE MAGNITUDE-
1053 FREQUENCY b VALUE. Bulletin of the Seismological Society of America, 72(5),
1054 1677–1687.

1055 Shibazaki, B., & Iio, Y. (2003). On the physical mechanism of silent slip events along the deeper
1056 part of the seismogenic zone. Geophysical Research Letters, 30(9), 1–4.
1057 https://doi.org/10.1029/2003GL017047

1058 Shimamura, K., Matsuzawa, T., Okada, T., Uchida, N., Kono, T., & Hasegawa, A. (2011).
1059 Similarities and differences in the rupture process of the M~ 4.8 repeating-earthquake
1060 sequence off Kamaishi, northeast Japan: comparison between the 2001 and 2008 events.
1061 Bulletin of the Seismological Society of America, 101(5), 2355–2368.

1062 Sibson, R. H. (1992). Implications of fault-valve behaviour for rupture nucleation and
1063 recurrence. Tectonophysics, 211(1–4), 283–293. https://doi.org/10.1016/0040-
1064 1951(92)90065-E

1065 Smith, D. E., & Dieterich, J. H. (2010). Aftershock sequences modeled with 3-D stress
1066 heterogeneity and rate-state seismicity equations: Implications for crustal stress
1067 estimation. In Seismogenesis and Earthquake Forecasting: The Frank Evison Volume II
1068 (pp. 213–231). Springer.

1069 Smith, D. E., & Heaton, T. H. (2011). Models of stochastic, spatially varying stress in the crust
1070 compatible with focal-mechanism data, and how stress inversions can be biased toward
1071 the stress rate. Bulletin of the Seismological Society of America, 101(3), 1396–1421.
1072 https://doi.org/10.1785/0120100058

1073 Suwa, Y., Miura, S., Hasegawa, A., Sato, T., & Tachibana, K. (2006). Interplate coupling
1074 beneath NE Japan inferred from three-dimensional displacement field. Journal of
1075 Geophysical Research: Solid Earth, 111(B4).

Suyehiro, S. (1966). Difference between aftershocks and foreshocks in the relationship of magnitude to frequency of occurrence for the great Chilean earthquake of 1960. Bulletin of the Seismological Society of America, 56(1), 185–200.

Tajima, F., & Kanamori, H. (1985). Global survey of aftershock area expansion patterns. Physics of the Earth and Planetary Interiors, 40(2), 77–134.

Tamaribuchi, K., Yagi, Y., Enescu, B., & Hirano, S. (2018). Characteristics of foreshock activity inferred from the JMA earthquake catalog. Earth, Planets and Space, 70(1), 90.

Tormann, T., Wiemer, S., Enescu, B., & Woessner, J. (2016). Normalized rupture potential for small and large earthquakes along the Pacific Plate off Japan. Geophysical Research Letters, 43(14), 7468–7477.

Tse, S. T., & Rice, J. R. (1986). Crustal earthquake instability in relation to the depth variation of frictional slip properties. Journal of Geophysical Research: Solid Earth, 91(B9), 9452–9472.

Uchida, N., Hasegawa, A., Matsuzawa, T., & Igarashi, T. (2004). Pre-and post-seismic slow slip on the plate boundary off Sanriku, NE Japan associated with three interplate earthquakes as estimated from small repeating earthquake data. Tectonophysics, 385(1–4), 1–15.

Uchida, N., & Matsuzawa, T. (2013). Pre-and postseismic slow slip surrounding the 2011 Tohoku-oki earthquake rupture. Earth and Planetary Science Letters, 374, 81–91.

Uchida, N., & Bürgmann, R. (2019). Repeating earthquakes. Annual Review of Earth and Planetary Sciences, 47.

Uchida, N., Matsuzawa, T., Hasegawa, A., & Igarashi, T. (2003). Interplate quasi-static slip off Sanriku, NE Japan, estimated from repeating earthquakes. Geophysical Research Letters, 30(15).

Uchida, N., Yui, S., Miura, S., Matsuzawa, T., Hasegawa, A., Motoya, Y., & Kasahara, M. (2009). Quasi-static slip on the plate boundary associated with the 2003 M8. 0 Tokachi-oki and 2004 M7. 1 off-Kushiro earthquakes, Japan. Gondwana Research, 16(3–4), 527–533.

Urata, Y., Yoshida, K., Fukuyama, E., & Kubo, H. (2017). 3-D dynamic rupture simulations of the 2016 Kumamoto, Japan, earthquake 4. Seismology. Earth, Planets and Space, 69(1), 150. https://doi.org/10.1186/s40623-017-0733-0

Vassiliou, M. S., & Kanamori, H. (1982). The energy release in earthquakes. Bulletin of the Seismological Society of America, 72(2), 371–387.

Venkataraman, A., & Kanamori, H. (2004). Observational constraints on the fracture energy of subduction zone earthquakes. Journal of Geophysical Research: Solid Earth, 109(5). https://doi.org/10.1029/2003JB002549

Vidale, J. E., & Shearer, P. M. (2006). A survey of 71 earthquake bursts across southern California: Exploring the role of pore fluid pressure fluctuations and aseismic slip as drivers. Journal of Geophysical Research: Solid Earth, 111(5), 1–12. https://doi.org/10.1029/2005JB004034

Waldhauser, F., & Ellsworth, W. L. (2000). A Double-difference Earthquake location algorithm: Method and application to the Northern Hayward Fault, California. Bulletin of the Seismological Society of America, 90(6), 1353–1368. https://doi.org/10.1785/0120000006

Wang, L., Hainzl, S., Zöller, G., & Holschneider, M. (2012). Stress-and aftershock-constrained joint inversions for coseismic and postseismic slip applied to the 2004 M6. 0 Parkfield earthquake. Journal of Geophysical Research: Solid Earth, 117(B7).

Wessel, P., & Smith, W. H. F. (1998). New, improved version of generic mapping tools released. Eos, Transactions American Geophysical Union, 79(47), 579–579. https://doi.org/10.1029/98EO00426

Wesson, R. L. (1987). Modelling aftershock migration and afterslip of the San Juan Bautista, California, earthquake of October 3, 1972. Tectonophysics, 144(1–3), 215–229.

Woessner, J., Schorlemmer, D., Wiemer, S., & Mai, P. M. (2006). Spatial correlation of aftershock locations and on-fault main shock properties. Journal of Geophysical Research: Solid Earth, 111(B8).

Xue, L., Bürgmann, R., Shelly, D. R., Johnson, C. W., & Taira, T. (2018). Kinematics of the 2015 San Ramon, California earthquake swarm: Implications for fault zone structure and driving mechanisms. Earth and Planetary Science Letters, 489, 135–144. https://doi.org/10.1016/j.epsl.2018.02.018

Yabe, S., & Ide, S. (2018). Variations in precursory slip behavior resulting from frictional heterogeneity. Progress in Earth and Planetary Science, 5(1), 43.

Yabe, Y., Nakatani, M., Naoi, M., Philipp, J., Janssen, C., Watanabe, T., et al. (2015). Nucleation process of an M2 earthquake in a deep gold mine in South Africa inferred from on-fault foreshock activity. Journal of Geophysical Research: Solid Earth, 120(8), 5574–5594.

Yamanaka, Y., & Kikuchi, M. (2004). Asperity map along the subduction zone in northeastern Japan inferred from regional seismic data. Journal of Geophysical Research: Solid Earth, 109(B7).

Yoshida, K., Hasegawa, A., & Okada, T. (2015). Spatially heterogeneous stress field in the source area of the 2011 Mw 6.6 Fukushima-Hamadori earthquake, NE Japan, probably caused by static stress change. Geophysical Journal International, 201(2), 1062–1071. https://doi.org/10.1093/gji/ggv068

Yoshida, K., & Hasegawa, A. (2018a). Hypocenter Migration and Seismicity Pattern Change in the Yamagata-Fukushima Border, NE Japan, Caused by Fluid Movement and Pore Pressure Variation. Journal of Geophysical Research: Solid Earth, 123(6), 5000–5017. https://doi.org/10.1029/2018JB015468

Yoshida, K., & Hasegawa, A. (2018b). Sendai-Okura earthquake swarm induced by the 2011 Tohoku-Oki earthquake in the stress shadow of NE Japan: Detailed fault structure and hypocenter migration. Tectonophysics, 733(August 2017), 132–147. https://doi.org/10.1016/j.tecto.2017.12.031

Yoshida, K., Hasegawa, A., & Okada, T. (2016a). Heterogeneous stress field in the source area of the 2003 M6.4 Northern Miyagi Prefecture, NE Japan, earthquake. Geophysical Journal International, 206(1), 408–419. https://doi.org/10.1093/gji/ggw160

Yoshida, K., Hasegawa, A., & Yoshida, T. (2016b). Temporal variation of frictional strength in an earthquake swarm in NE Japan caused by fluid migration. Journal of Geophysical Research: Solid Earth, 121(8), 5953–5965. https://doi.org/10.1002/2016JB013022

Yoshida, K., Hasegawa, A., Okada, T., Iinuma, T., Ito, Y., & Asano, Y. (2012). Stress before and after the 2011 great Tohoku-oki earthquake and induced earthquakes in inland areas of eastern Japan. Geophysical Research Letters, 39(3). https://doi.org/10.1029/2011GL049729

Yoshida, K., Hasegawa, A., Okada, T., & Iinuma, T. (2014). Changes in the stress field after the 2008 M7.2 Iwate-Miyagi Nairiku earthquake in northeastern Japan. Journal of Geophysical Research: Solid Earth, 119(12), 9016–9030. https://doi.org/10.1002/2014JB011291

Yoshida, K., Saito, T., Urata, Y., Asano, Y., & Hasegawa, A. (2017). Temporal Changes in Stress Drop, Frictional Strength, and Earthquake Size Distribution in the 2011 Yamagata-Fukushima, NE Japan, Earthquake Swarm, Caused by Fluid Migration. Journal of Geophysical Research: Solid Earth, 122(12), 10,379-10,397. https://doi.org/10.1002/2017JB014334

Yoshida, K., Hasegawa, A., Yoshida, T., & Matsuzawa, T. (2019a). Heterogeneities in stress and strength in tohoku and its relationship with earthquake sequences triggered by the 2011 M9 Tohoku-Oki earthquake. Pure and Applied Geophysics, 176(3), 1335–1355.

Yu, W. (2013). Shallow-focus repeating earthquakes in the Tonga--Kermadec--Vanuatu subduction zones. Bulletin of the Seismological Society of America, 103(1), 463–486.

Yukutake, Y., Ito, H., Honda, R., Harada, M., Tanada, T., & Yoshida, A. (2011). Fluid-induced swarm earthquake sequence revealed by precisely determined hypocenters and focal mechanisms in the 2009 activity at Hakone volcano, Japan. Journal of Geophysical Research: Solid Earth, 116(4), 1–13. https://doi.org/10.1029/2010JB008036